Three-Dimensional Quantitative Cerenkov Luminescence Imaging

By

Anton Ajne

ABSTRACT

Nearly a century ago Pavel Cerenkov predicted, and verified, that charged particles travelling at high velocities trough dielectric media emits light in the UV-NIR range. As it turns out, several β-emitting radioisotopes produces β-particles of sufficient energy to induce this Cerenkov emission in tissue like media. In 2009 Cerenkov luminescence imaging (CLI) was proposed as an optical imaging modality, relying on the detection of the Cerenkov radiation emitted from radioisotopes inside a subject. The technique share a lot similarities with PET, and it is very common to use PET probes for CLI. Several studies has compared the two methods and for superficial measurements good agreement has been found. As most optical methods CLI is however very depth limited and its potential applications are primarily in a pre-clinical environment.

In this work a forward model for the emission and propagation of Cerenkov radiation from β-emitting isotopes is presented. The model is based on the continuous slowing down approximation for the interactions of β-particles with the tissue. The theory of Frank and Tamm is employed for the emission of Cerenkov radiation and the radiative transport equation for the propagation of the Cerenkov photons.

Based on the forward model an inverse model for the reconstruction of the spatial distribution of the radioisotope from external measurements is presented. The inverse model is formulated as an optimization problem, where the difference between predicted Cerenkov intensity from the forward model and measurements are minimized. The optimization is performed iteratively using the Levenberg-Marquardt algorithm.

Validation of the underlying assumptions and approximations is performed by comparison to Monte Carlo simulations. The performance of the models and their implementation was assessed through simulations and to some extent experimental studies. The initial results indicates that the forward model is working as intended. While reconstruction of simulated data produced reasonable results, the reconstruction of the experimental measurements were mediocre at best.

POPULÄRVETENSKAPLIG SAMMAN-FATTNING

Molekylära avbildningsmetoder har gjort det möjlighet att följa biologiska processer på molekyl- och cellnivå. SPECT och PET är etablerade tekniker för molekylär avbildning som används dagligen inom både sjukvård och forskning. Andra metoder existerar, så som magnetröntgen och ultraljud, men dessa har mer begränsade tillämpningar inom ämnet och kommer därför inte diskuteras närmare. I SPECT och PET introduceras ett radioaktivt preparat i objektet som ska avbildas och därefter mäter man den högenergetiska gammastrålningen som avges då det radioaktiva preparatet sönderfaller. Från dessa mätningar beräknar man sedan preparatets fördelning i objektet. Ofta är man intresserad av att avbilda någon specifik process eller områrde. I dess fall fäster man ofta preparatet på en molekyl som söker sig till processen eller området av intresse.

Gemensamt för SPECT och PET är att detektorerna (gammakamerorna) som används är stora och relativt dyra, vilket ofta begränsar antalet maskiner på ett institut. Undersökningen tar också relativt lång tid, ca 15-30 min beroende på vad som ska avbildas. I de flesta fall är det dessutom endast möjligt att avbilda ett objekt i taget. Detta tillsammans med ett begränsat antal maskiner innebär en hård begränsing på antal undersökningar som kan utföras under en viss tid. För forskningssyften, särskilt vid djurförsök, kan detta vara mycket begränsande. Ofta vill man följa en stor population och göra mätningar på samtliga individer vid ungefär samma tidpunkt. De tidigare nämnda restriktionerna kan alltså innebära en begränsning för kvalitén på dessa typer av studier.

En möjlighet för att dels komma runt detta problem, men också öppna upp nya tillämpningar inom molekylär avbildning, är optiska avbildningstekniker. I dagsläget finns det en uppsjö av optiska metoder under utveckling. Många av dem bygger på olika principer men de har alla den gemensamma nämmnaren ljus i det ultravioletta, synliga och infraröda området. Denna typ av ljus är lätt att mäta jämfört med gammastrålning, i princip skulle en vanlig digitalkamera kunna användas. I praktiken används dock något mer sofistikerade kameror då ljuset som ska mätas ofta är mycket svagt. I många fall är det dessutom möjligt att utföra mätningar på flera objekt samtidigt. Jämfört med gammastrålningen som används vid SPECT och PET så har det optiska ljuset dessutom mycket mindre skadlig inverkan på biologisk vävnad. Dessa fördelar kommer till kostnaden av att det optiska ljuset inte kan färdas några längre sträckor i vävnad innan det släcks ut. Gammastrålning kan passera genom en hel kropp med liten inverkan på dess riktning och intensitet. Optiskt ljus kommer snabbt att förlora sin ursprungliga riktning och dessutom att vara helt utsläckt efter, i bästa fall, bara ett par centimeter.

En relativt ny optisk metod, den första artikeln som behandlade den publicerades 2009, är Cerenkov luminiscens avbildning (Cerenkov luminescence imaging på engelska). Metoden bygger på Cerenkovstrålning, vilket är det optiska ljuset som avges då elektriskt laddade partiklar färdas med hög hastighet genom vissa medium. Vanligtvis används radioaktiva preparat som vid sönderfall avger laddade partiklar med tillräckligt hög hastighet för att producera Cerenkovstrålningen. Många av de preparat som används vid PET undersökningar uppfyller dessa specifikationer. Detta har snabbat på utvecklingen av metoden eftersom att det redan från början fanns godkända preparat till hands. PET är också den metod som Cerenkov avbildning jämförts mest med och flertalet studier har visat god överenstämmelse mellan dem vid ytliga mätningar.

Potentiella tillämpningar av Cerenkov avbildning är också främst som substitut till PET vid ytliga undersökningar. För kliniska syften har bland annat möjligheter för sköldkörtelundersökningar och vävnadsklassifikation under kirurgiska ingrepp diskuterats. PET undersökningar kräver att det radioaktiva preparatet som används avger positroner vid sönderfall, detta krav finns inte vid Cerenkov avbildning, där även preprat som avger elektroner kan användas. För rena avbildningssyften är detta av litet intresse då preparatet som används bara ska ge kontrast och dess exakta karaktär inte är av större intresse. Vid strålbehandlingar, då en patient ges ett radioaktivt preparat för behandling, är preparatets karaktär å andra av största intresse, eftersom att det avgör vilken effekt behandlingen får. Här skulle alltså Cerenkov avbildning kunna användas för att monitorera och evaluera strålbehandling där preparat som avger elektroner används. Vilket inte alltid är görbart med SPECT eller PET.

I den här rapporten presenteras en Cerenkov metod för molekylär avbildning. Den underliggande teorin för Cerenkov fenomenet och transport av ljus genom vävnad behandlas. Utifrån denna teori är en modell för den uppmätta strålningen från ett radioaktiva preparat presenterad. Baserat på denna modell är en avbildningalgoritm uppbyggd som utifrån mätningar av Cerenkovstrålning försöker återskapa det radioaktiva preparatets utbredning i objektet. Båda modellerna har testats med datorsimulationer men också experimentellt genom mätningar på vävnadsliknande plastfantomer.

CONTENTS

1 INTRODUCTION

1.1 Molecular imaging

Molecular imaging is the common name for non-invasive techniques which aims to visualize biochemical interactions and events at a molecular or cellular level. In clinics it is used for both diagnostic and therapeutic purposes and in preclinical studies it is an invaluable tool for researchers. Although a handful of modalities are commercially available there is much interest in new methods and a large amount of research is put into it.

Commonly molecular imaging is performed by introducing a marker, which is traceable in some sense, into the subject of interest. Depending on the application the marker may be administered in different ways. If a specific area or process is of interest the marker can be attached to a specific molecule, known as a tracer, which accumulates in the desired region or is involved in the particular process. But the marker may also be injected freely into the subject. How the marker is detected differs between techniques and in some cases external excitation of the marker is required.

In this thesis a relatively new, experimental molecular imaging modality known as Cerenkov luminescence imaging is investigated. A quantitative model is developed and tested to asses its potential for molecular imaging.

1.1.1 Clinical modalities

The most common clinical molecular imaging techniques today are single photon emission computed tomography (SPECT), positron emission tomography (PET), magnetic resonance imaging (MRI) and ultrasound imaging. Even though they are all commercially available and commonly used in clinics, there is still a lot work involving them in the preclinics, both for further development of them and as imaging tools in other studies.

SPECT and PET have many similarities, both uses radioactive isotopes as markers, γ-emitters for SPECT and positron emitters for PET and the detection of the marker is in both cases performed with a gamma camera. In SPECT the emitted γ-photons from the radioactive decay is measured. PET on the other hand relies on the detection of γ-photon pairs produced from annihilations of emitted positrons and electrons in the subject. By changing the location of the camera a set of images is produced from which the spatial distribution of the marker is reconstructed. Due to the use of γ-rays for detection these methods have good imaging capabilities regardless of depth. Both methods have a high sensitivity, meaning that it is

1

possible to detect small amounts of the marker. Major limitations to SPECT and PET is bulky and expensive equipment, the procedure also takes quite some time and only one subject can be imaged at a time [1]. SPECT and particularly PET share similarities with CLI, both in methodology and application. For this reason it is interesting to use them for comparison and as a benchmark.

MRI is a very versatile imaging technique where both anatomical and molecular information can be reconstructed. MRI exploits atomic nuclei with a non-zero magnetic moment as markers. Under the influence of an external magnetic field these nuclei align either parallel or anti-parallel to the field. These two populations differ by a small fraction and this is used for detection. The difference in population depends on the external field strength but is still very small even in the 1 Tesla range, which is common in clinical machines. This causes MRI to have rather poor sensitivity, compared to SPECT and PET the marker concentration must be several orders of magnitude higher to be detectable [1]. Also it does not relate closely to CLI and will therefore not be discussed any further.

Ultrasound imaging is a well established imaging modality but its applicability for molecular imaging have not been investigated until recent years. High frequency sound waves are used to probe the subject and shifts in the properties (phase, frequency, amplitude) of the reflected waves are used to reconstruct the probed volume. Different markers exist and is generally divided into microbubble agents and non-microbubble agents. The microbubbles are micrometre sized gas bubbles surrounded by a shell, and are designed to give a clear echo of the sound wave yielding a high sensitivity. The non-microbubbles are typically smaller, 10-1000 nanometre, and either solid or liquid. The smaller size gives them the ability to reach locations microbubbles can not. They will however reflect a weaker echo and thus results in a lower sensitivity [2]. Ultrasound imaging is relatively cheap and the acquisition time is very short, several images can be produced per second, making real-time imaging of the subject possible. The use of sound does however limit the depth which is possible to probe.

1.1.2 Optical imaging

There is an extensive number of preclinical molecular imaging methods, a subgroup of these which has fetched much interest in recent years is the optical imaging techniques. The common part of these are the use of light in the ultraviolet, visible and near infra-red (UV-VIS-NIR) range. Even in this subgroup the amount of methods is far to great to cover here and only a small selection will be mentioned. Optical techniques typically has a higher throughput, which basically indicates a higher sensitivity, than SPECT/PET and the instrumentation required is often cheaper. The major limitation for optical imaging is the strong

attenuation and scattering of light in the optical range. Where γ-photons usually can pierce straight through a human body, light in the optical light will have its original direction completely distorted after a few millimetres and its intensity reduced below the detection threshold after a few centimetres. These effects are strongly dependant on the type of tissue the light propagates through and also the wavelength of the light. As the optical light has very limited range in tissue it can often only be measured at certain parts of the subject. Compared to SPECT/PET where measurements are available at all parts of the subject the amount of data will generally be more limited.

Fluorescence imaging is a very popular optical imaging technique which uses fluorophores as markers. The fluorophore is introduced into the subject, possibly attached to a targeting agent, and then excited by some internal or external light source. The emitted fluorescent light is measured and from this measurement the distribution of the fluorophore is calculated. This method is rather versatile as different fluorophores have different absorption and emission characteristics.

Bioluminescence imaging exploits the bioluminescence phenomena, where certain genes expresses substances which through chemical processes emits light. This occurs naturally in some species, fireflies being one of the most famous, but the genes can also be implanted into other specimen. Usually the genes are implanted in such a way that they are expressed under some circumstance of interest. Imaging is performed by measuring the luminescence and calculation a three-dimensional representation of the bioluminescence source-distribution.

1.1.3 Cerenkov luminescence imaging

The term Cerenkov luminescence imaging (CLI) was coined by Robertson *et al.* in 2009 when they studied the Cerenkov emission from the PET probe ^{18}F-FDG in well plates and a xenograft tumour in a mouse [3]. This method is based on the radiation produced from charged particles travelling at high velocities through a medium, known as Cerenkov radiation. The charged particles are produced from the decay of some radioactive isotope and from the measurement the distribution of the isotope is imaged. In principle an external source of charged particles could be used to induce the Cerenkov radiation as well, but for the purpose of CLI this is not of interest as very little molecular information would be recovered. In practice it is mainly β-emitting isotopes that are useful for CLI as heavier particles require far to much energy to reach the velocities needed to produce Cerenkov radiation. Conveniently, many of the β^+-emitters used for PET has proven to be useful for CLI. The main difference between PET and CLI is thus the origin of the measured radiation, positron-electron annihilation for PET and Cerenkov radiation emitted by the β-particle as it travels through the subject for CLI. Due to this difference

the reconstruction algorithms and detection equipment also differ. The Cerenkov radiation is usually measured with a CCD, which in general is much smaller and cheaper than the gamma cameras required for PET. In CLI electron emitters may also be used as markers, giving it a larger range of available markers compared to PET.

CLI is still a fairly experimental method and is predominantly used in small animal or *in vitro* studies. For *in vivo* CLI the radioactive marker is usually intravenously injected, often attached to a tracer designed to accumulate in a specific part of the subject, like a tumour. As most other optical imaging techniques CLI is very depth limited, perhaps even more so than some other methods due to the Cerenkov radiation being rather weak by nature.

1.2 Applications of CLI

Due to the very limited depth at which CLI can be used, its potential clinical applications are very limited. Instead most of its applications is in a pre-clinical environment.

1.2.1 CLI as an alternative to SPECT/PET

CLI and SPECT/PET are basically different methods designed for the same purpose, to image radioactive decay. Many of the proposed applications of CLI are also, in some sense, as replacement for SPECT/PET. The performance of SPECT/PET also provides a natural frame of reference for assessment of CLI.

A common argument for CLI is its potentially higher throughput compared to SPECT/PET, which would imply a higher rate of data acquisition, implying that a shorter acquisition time would be required. In SPECT each γ-decay produces one photon and in PET each β^+-emission produces a photon pair, but due to the design of PET it will only be considered as a single detection event. Both SPECT and PET thus has an upper limit of one detection per decay, and in practice lower since not all photons are captured. The number of Cerenkov photons produced per β-decay depends on the initial energy of the β-particle and also on the medium in which the decay occurs. The amount of detected radiation will also strongly depend on the source-detector distance. The Cerenkov radiation is emitted in a continuous spectrum, which is quite different from SPECT/PET where the γ-photons has a fixed energy. The detection for CLI will thus further depend on the camera's ability to detect light at different wavelengths. Ross presented a table of the Cerenkov radiation produced by electrons in water, which in general yields less Cerenkov photons than in tissue, in the 250-600 nm range [4]. In

figure 1.1 these values are displayed as a function of the electron energy. Clearly
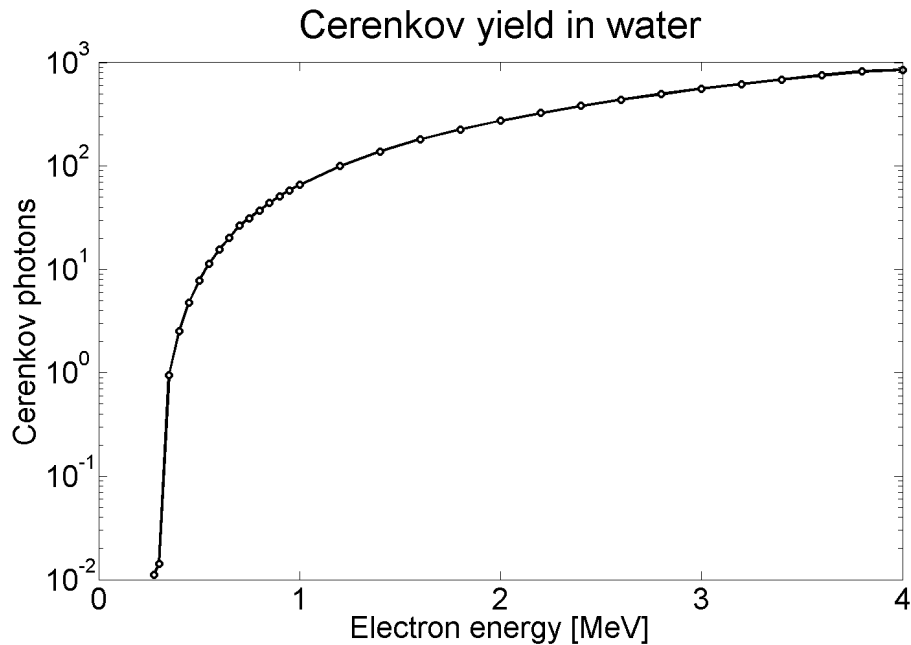
Figure 1.1: Calculated Cerenkov photons emitted from an electron travelling through water in the 250-600 nm spectral band.

the amount of Cerenkov radiation grows quickly with the electron energy. For electrons with initial energy of around 0.5 MeV only a few photons are emitted, while hundreds are emitted if the energy is increased to 1.5 MeV. These energies are within reasonable bounds for medical use, there are several PET probes which produces β-particles with energies up to a few MeV. For high energy β-emitters it is thus reasonable to expect several detections per decay, and thus a higher throughput. For low energy emitters this is however more questionable.

It has been argued that CLI potentially could give a higher spatial resolution than PET. This is due to the fact that the radiation measured in PET does not originate from the marker itself, but from the annihilation of positrons emitted by the marker. The annihilations occur when the emitted positrons interacts with electrons in the subject, which occurs at a random distance from the decay. The Cerenkov radiation on the other hand is continuously emitted by the particle, furthermore the radiation is stronger closer to the decay. If the reconstruction could be performed to perfectly recover the origin of the radiation, CLI could thus be expected to outperform PET. However, perfect reconstructions is not feasible and it is questionable weather this effect comes into play or not.

The most important advantage of CLI would still probably be the simpler equipment required. SPECT and PET are rather expensive methods and CLI could possibly increase the availability of molecular imaging to researchers.

Several studies has assessed the performance of CLI in different settings. Both *in vitro* and *in vivo* experiments with different radioisotopes as markers has been conducted. Despite the different settings the conclusion has been similar, it is indeed possible to detect the Cerenkov radiation and the reconstruction of the radionuclei correlate well with SPECT/PET [5–14]. The spatial resolution found in these studies has been comparable to the resolution of SPECT/PET.

1.2.2 Other proposed applications of CLI

A possible clinical applications of CLI is monitoring of the thyroid gland. This could be possible due to the thyroid being located close to the skin. Initial studies in mice has shown promising results CLI [7, 15]. Cerenkov imaging of the thyroid in a human after treatment with ^{131}I, possibly the first Cerenkov image of a human, has also been performed [16], proving its clinical potential.

Due to the much smaller detection device and shorter acquisition time for CLI compared to PET it has been proposed as an intraoperative guidance tool. With current techniques, often SPECT or PET, surgeons have to relay on pre-operative images. CLI (and other OI techniques) on the other hand could potentially be used during surgery to provide updated images during the procedure. Studies show that, although more work needs to be done, it is feasible [17, 18].

CLI has great potential for assessment of radiation therapy. For imaging purposes the characteristics of the marker is normally not that important, as long as it provides good contrast. For radiation therapy however the characteristics of the radiation source is crucial for the outcome of the treatment. Neither SPECT nor PET can directly image electron emitters and therefore the assessment of their potential for therapy is somewhat more complicated then gamma or positron emitters. The possibility to image electron emitters with CLI would offer an easier way of assessing the potential for such isotopes [11, 12].

The possibility to image α-emitters with CLI has also been discussed. The α-particles themselves would not be energetic enough to produce Cerenkov radiation, over 1 GeV is required and the energy of emitted α-particles will typically be below 10 MeV. However it is common that the nucleus undergoes several rapid decays after the initial α-decay. These subsequent decays may be of different type, and often some of them are β or γ-decays. These β-particles may be energetic enough to be useful for CLI, it may also be possible for the γ-rays to produce high energy electrons through Compton scattering. While it is possible for Cerenkov

radiation to be produced in this way, the time delay between decays and the number of different isotopes makes the reconstruction problem much harder [19].

Another interesting possibility is the use of Cerenkov radiation as a source for excitation light. A few studies has investigated Cerenkov radiation as excitation for fluorescent imaging [20–22]. It has also been proposed as excitation for photosensitizers during photo dynamic therapy [23]. The advantage with Cerenkov radiation over conventional light sources would be the production of light within the subject, and it should thus not be as heavily attenuated. While these applications does not directly involve CLI it could be of interest to monitor the excitation field, as it heavily affects the results, which could be done using CLI. In these cases the Cerenkov radiation is not used for the actual imaging and an external β-source is thus a feasible alternative to radioactive isotopes [24, 25].

1.3 Purpose

CLI has emerged as a promising new modality for molecular imaging of radioactive decay *in vivo*. In this work the underlying theory for the Cerenkov phenomena and and the transport of the produced radiation through tissue is presented. This theory is used to formulate a mathematical model which quantifies the amount of Cerenkov radiation produced in a subject. From this model a reconstruction algorithm is presented, which estimates the distribution of the radioactive marker.

The primary purpose of this work is thus to present a theoretical CLI framework. The results presented will mainly be used as validation for this particular framework rather than assessing CLI as a method.

1.4 Aims

In this thesis a forward model for the propagation of Cerenkov radiation will be constructed. This model should for a given subject with known properties as well as a known distribution of a radionuclide calculate the stationary distribution of Cerenkov radiation within the subject as well as the radiation leaving through its boundaries. Key components to this model is the calculation of emitted radiation from a radionuclide and the propagation of it through the subject.

Based on the forward model an inverse model to reconstruct the activity distribution from boundary measurements of the Cerenkov radiation will be presented. Primarily good reconstruction of the location and shape of the radionuclide distribution is of interest.

1.5 Assumptions

Optical imaging is a notoriously hard subject and CLI is no exception, for this reason several approximations and simplifying assumptions are made.

- The Cerenkov radiation produced from a β-particle depends on its energy, which in turn is stochastic. As a deterministic approach is taken expected values are used wherever necessary.

- Scattering of β-particles is neglected.

- The Cerenkov radiation is assumed to be isotropically emitted.

- The optical characteristics of the subject is assumed to be accurately modelled by its refractive index, absorption and scattering coefficients, anisotropy factor and scattering phase function. Further more the scattering phase function is assumed to be well approximated by the Henyey-Greenstein phase function.

- The equation governing the transport of light through the subject is assumed to be well estimated by a low-order simplified spherical harmonic approximation.

2 THEORY

2.1 Cerenkov radiation

Cerenkov radiation is the light which can be observed when highly energetic charged particles travel through certain materials. A common example of Cerenkov radiation is the blue light surrounding a nuclear reactor submerged in water. It was explained by Pavel Alekseyevich Cerenkov in the 1930s, for which he was awarded the 1958 Nobel price in physics.

2.1.1 Emission

In a dielectric medium the electric field surrounding a charge will polarize nearby atoms or molecules. If the charge is moving the atoms or molecules will return to their ground states as the charge passes them by. During the transition of the atoms or molecules to their ground states photons are emitted. However, if the charge is moving at a low velocity the photons emitted will interfere destructively and no radiation is observed at a distance. If the charge on the other hand travels at a high velocity there will be constructive interference at a certain angle relative to the direction of the charge. This results in a light cone centred around the charge and it is this light which is referred to as Cerenkov radiation [26]. The angle θ at which photons are emitted is given by Cerenkov's relation

$$\cos \theta = \frac{1}{\beta n}. \tag{2.1}$$

Here β is the speed of the charge divided by the speed of light in vacuum and n is the refractive index of the medium. The threshold velocity of the charge for Cerenkov emission to occur is the phase velocity of light in the medium, which can be stated as

$$\beta n > 1.$$

Cerenkov radiation can consequently only occur in dielectric media with a refractive index greater than unity. The requirement for the charge to be superluminal can also be stated as a requirement for the charge to travel faster than its own electromagnetic bow wave.

2.1.2 Frank-Tamm theory

The amount Cerenkov radiation emitted per unit path length travelled by a particle carrying a charge q is given by the Frank-Tamm formula [26]

$$\frac{dE}{dx} = \frac{q^2}{c^2} \int_{\beta n > 1} \left(1 - \frac{1}{\beta^2 n^2} \right) \omega \, d\omega. \tag{2.2}$$

The integral in 2.2 might seem divergent as ω goes to infinity but in practice the refractive index will go to (or even below) unity for high frequencies, making the Cerenkov condition impossible to satisfy. In most cases the emitted energy in a certain spectral band is of interest, rather than the total output. This is easily achieved by limiting the integral in 2.2 to the interval $[\omega_1, \omega_2]$ of interest, given that the Cerenkov condition holds in the interval. An extension to the Frank-Tamm theory was developed by Budini, which characterizes the medium by a complex dielectric function rather than the refractive index. This theory results in convergent expression for the Cerenkov emission [27]. However in the spectral range of interest for CLI the original expression 2.2 has been found to describe the Cerenkov emission well [28, 29].

In optical imaging applications it is commonly preferred to work with wavelength rather than angular frequency. The corresponding formulation is found by using the relation
$$\omega = \frac{2\pi c}{\lambda}.$$
This yields the wavelength formulation of the Frank-Tamm formula

$$\frac{dE}{dx} = 4\pi^2 q^2 \int_{\lambda_1}^{\lambda_2} \left(1 - \frac{1}{\beta^2 n^2}\right) \frac{1}{\lambda^3}\, d\lambda, \tag{2.3}$$

where λ_1 corresponds to ω_2 and λ_2 to ω_1, thus $\lambda_1 < \lambda_2$ (note the change of order in integration limits). The particles velocity does not depend on λ and if the refractive index can be assumed to be constant in the interval $[\lambda_1, \lambda_2]$ 2.3 can be further simplified as

$$\frac{dE}{dx} = 4\pi^2 q^2 \left(1 - \frac{1}{\beta^2 n^2}\right) \int_{\lambda_1}^{\lambda_2} \frac{1}{\lambda^3}\, d\lambda = 2\pi^2 q^2 \left(1 - \frac{1}{\beta^2 n^2}\right)\left(\frac{1}{\lambda_1^2} - \frac{1}{\lambda_2^2}\right). \tag{2.4}$$

From 2.4 it can be seen that the spectrum of the Cerenkov radiation is proportional to λ^{-3}, that is

$$\frac{dE}{d\lambda} \propto \frac{1}{\lambda^3}. \tag{2.5}$$

In this formulation of the Frank-Tamm theory units are chosen so that the permittivity factor $4\pi\varepsilon_0 = 1$ and dimensionless. From the definition of the fine structure constant α this implies that other units should be chosen so that

$$e^2 = \alpha\hbar c, \tag{2.6}$$

where e is the fundamental electric charge, $\hbar$ the reduced Plank's constant and c the speed of light in vacuum.

10

2.2 β-decay

Radioactive decay is the natural process through which unstable atomic nuclei is converted to more stable ones. During β-decay a proton in a nucleus is converted to a neutron, or vice versa, changing its atomic number by one while leaving its mass number unchanged. To maintain the conservation of electric charge during the conversion an electron or positron is emitted. The two modes of decay are often distinguished by the abbreviations β^--decay, which indicates the emission of an electron, and β^+-decay which indicates that a positron is emitted. Along with the β-particle a neutrino or anti-neutrino is emitted. The general form of an element A transitioning to another element B through β-decay is thus

$$_Z^N\text{A} \rightarrow {}_{Z\pm1}^N\text{B} + \beta + \nu. \tag{2.7}$$

2.2.1 Energy of emitted β-particles

The difference between the energy of the parent and the daughter nucleus determines the total energy of the β-particle and the neutrino. Apart from the fact that each particle must carry at least its rest mass in energy, there is no restriction as to how the energy is distributed. The kinetic energy of emitted β-particles will thus form a continuous probability distribution between 0 and some maximum value (and likewise for the neutrino). The probability distribution as well as the maximum kinetic energy varies between different radioactive isotopes and is governed by Fermi theory [30]. In this work energy distributions from the RADAR decay database has been used [31].

2.2.2 β-range and stopping power

When β-particles travel through a medium they gradually lose their energy through different interaction. Two types of interactions occur, inelastic collisions which includes ionization or excitation of atoms and molecules. The other type is elastic interactions which is Bremsstrahlung [32, 33]. These interactions occur at discrete times and the loss of energy will thus be in discrete steps.

A common strategy to model these rather complicated interactions is to assume that the particle looses its energy continuously at some average rate with respect to the available interactions. This is known as the continuous slowing down approximation (CSDA). The average rate of energy loss per unit path length is referred to as the stopping power $S(E)$. The stopping power depends on the energy of the particle, as the probability of different interactions changes with the energy, and also on the medium. The stopping power is usually decomposed as a sum of

the stopping power due to collisions (inelastic interactions) and radiation (elastic interactions). The stopping power used in this work has been interpolated from ESTAR Stopping Power and Range Tables, provided by the National Institute of Standards and Technology [34].

With this model the energy loss is governed by the equation

$$\frac{dE}{dx} = -S(E), \quad E(0) = E_0,$$
(2.8)

where $E(x)$ is the kinetic energy of the particle and E_0 its initial kinetic energy.

In addition to losing energy the β-particles may have their direction of travel changed by the above mentioned interactions. This scattering has however been neglected due to the complexity of it.

In the Frank-Tamm theory it was the relative speed of the particle rather than its kinetic energy which was used to calculate the Cerenkov emission. From the relativistic expression of energy a conversion formula can be found as

$$\beta(x) = \left[1 - \left(\frac{E_0}{E(x) + E_0} \right)^2 \right]^{\frac{1}{2}},$$
(2.9)

where E_0 its rest mass of the particle (0.511 MeV for β-particles).

There is a small discrepancy between the stopping power for electrons and positrons [35, 36]. It is however small in the energy region of interest and will therefore not be considered and the ESTAR data for electrons will be used for positrons as well.

2.3 Cerenkov radiation from β-decay

To perform CLI the amount of Cerenkov radiation produced by a radioactive sample has to be assessed. This can be achieved by combining the Frank-Tamm theory and the CSDA model for emitted β-particles. Due to the random initial energy of the β-particles the emitted Cerenkov radiation will also be random. In any practical situation the sample will however contain a large number or radioactive nuclei and it is fair to assume that the emitted radiation will be close to its expected value.

2.3.1 Average Cerenkov radiation from a decay

From a known initial energy of a β-particle its energy as a function of path travelled is found through 2.8. By applying 2.9 the relative speed β as a function of path is obtained and by plugging it into 2.4 the rate of Cerenkov emission is

found. In a certain spectral band with known material properties the Cerenkov emission thus only depends on the initial β-energy. By calculating the expected Cerenkov emission with respect to a certain isotopes energy distribution, the average Cerenkov emission from a decay of that isotope is found. The expected value is given by

$$\mathbb{E}\left[E(r)\right] = 2\pi^2 e^2 dr \left(\frac{1}{\lambda_1^2} - \frac{1}{\lambda_2^2}\right) \int\limits_{E_{Cer}}^{\infty} \left(1 - \frac{1}{\beta(r)^2 n^2}\right) f(E_0)\, dE_0, \qquad (2.10)$$

where r is the distance along the trajectory from the decay, $f(E_0)$ the energy distribution and E_{Cer} the threshold energy for Cerenkov emission. Frequently it will be of interest to calculate the expected Cerenkov emission from a particle at a certain part of its trajectory. This can be calculated by integrating 2.10 over the region of interest,

$$\mathbb{E}[E(r_1, r_2)] = \int\limits_{r_1}^{r_2} \mathbb{E}\left[E(r)\right]\, dr. \qquad (2.11)$$

From 2.10 the expected Cerenkov emission along the trajectory of a β-particle is given. This trajectory is however unknown as the direction at which the β-particle is emitted at is random. Rather than 2.10 the expected Cerenkov emission at an arbitrary point $\boldsymbol{r}$ is the quantity of interest. Assuming the direction of the emitted β-particles is uniformly distributed and that the decay occurs in the origin this is expected value is

$$\mathbb{E}\left[E(\boldsymbol{r})\right] = \int_{4\pi} \mathbb{E}\left[E(|\boldsymbol{r}|)\right] \delta\left(1 - \boldsymbol{s}\cdot\frac{\boldsymbol{r}}{|\boldsymbol{r}|}\right)\frac{1}{4\pi}\, d\boldsymbol{s} = \frac{1}{4\pi}\mathbb{E}\left[E(|\boldsymbol{r}|)\right]. \qquad (2.12)$$

Here δ is a translated Dirac pulse which indicates that only trajectories through $\boldsymbol{r}$ will contribute to the emitted energy. The factor $\dfrac{1}{4\pi}$ is the uniform probability distribution for the β-particle directions.

In the case $\boldsymbol{r} = 0$, 2.12 breaks down. In the continuous case, where the subject consists of a continuum of points, this is not a problem. It is however convenient to have an expression for all points and as 2.10 is defined for $r = 0$, 2.12 is simply extended as

$$\mathbb{E}\left[E(\boldsymbol{r})\right] = \frac{1}{4\pi}\mathbb{E}\left[E(|\boldsymbol{r}|)\right] \quad \forall\, \boldsymbol{r}. \qquad (2.13)$$

The expected emission at an arbitrary point is thus only dependent on the distance from the decay, which is expected since isotropic decay is assumed. It can also be seen that by integrating 2.12 over all directions 2.10 is recovered, as expected.

Finally the expected emission is normalized with a volume element dV as it is often preferable to express a source in units of energy per volume. The expected Cerenkov source from a single decay is then

$$Q_{Cer}(\boldsymbol{r}) = Q_{Cer}(|\boldsymbol{r}|) = \frac{1}{4\pi} \frac{\mathbb{E}\left[E\left(|\boldsymbol{r}|\right)\right]}{dV}. \tag{2.14}$$

2.3.2 Cerenkov radiation from an activity distribution

The rate at which a radioactive sample decays at is measured by its activity. Activity is commonly given in units of Becquerel (Bq) which is decays per second in the sample. The activity measures the total decays within the sample and does not hold any spatial information about the distribution of the radioactive compound within the sample. In order to resolve the radioactive inhomogeneities in the sample the activity distribution (or density), which is given as activity per volume, has to be considered.

The Cerenkov source scales linearly with the number of decays, and therefore also linearly with activity. The total source from the activity distribution A will thus be the sum of the decay in each point weighted by Q_{Cer}

$$Q(\boldsymbol{r}) = \int A(\boldsymbol{r}')Q_{Cer}(|\boldsymbol{r} - \boldsymbol{r}'|)\, d\boldsymbol{r}', \tag{2.15}$$

which can also be formulated as a convolution in three dimensions. This is the average total emitted power per volume and is thus the expected Cerenkov source from A.

The source term 2.15 is isotropic, which might seem odd due to the specific angle Cerenkov radiation is emitted in. However in an activity distribution $Q(\boldsymbol{r})$ will receive contributions from decays at several locations. On average it might thus be reasonable to assume that the contributions will be given from all directions equally, which will result in isotropic Cerenkov emission. Furthermore biological tissue is strongly scattering, implying that any directional dependence of the source will be suppressed.

14

2.4 Light transport in tissue

For a photon in the UV-IR range travelling through matter, there are two kinds of interaction to be considered. Absorption of the photon and scattering, which causes the photon to change its direction with all of its energy preserved.

2.4.1 Absorption

Certain molecules, called chromophores, have the ability to absorb light. This ability to absorb is usually wavelength dependent and can be characterized by a absorption coefficient $\mu_a(\lambda)$. The absorption coefficient determines the rate at which light travelling through a medium loses its intensity, governed by the Beer-Lambert law

$$I(x) = I_0 e^{-\mu_a(\lambda)x}. \tag{2.16}$$

In a composite material the absorption coefficient will be a weighted sum of each of the constituent chromophores absorption coefficients

$$\mu_a = \sum_i \mu_{a_i} f_i.$$

The weights f_i are the volume fractions of the chromophores in units of volume chromophore per volume medium, and is thus dimensionless.

In biological tissue the most influential chromophores are oxygenated haemoglobin (HbO$_2$), deoxygenated haemoglobin (Hb), water and lipids. Instead of specifying the volume fraction of both kinds of haemoglobin it is common to specify the total volume fraction of blood B and use the blood oxygen saturation S to distinguish them. This gives an absorption coefficient for the tissue

$$\mu_a = \mu_{a_{\text{HbO}_2}} BS + \mu_{a_{\text{Hb}}} B(1 - S) + \mu_{a_{\text{H}_2\text{O}}} W + \mu_{a_{\text{lipid}}} L, \tag{2.17}$$

where W and L are the water and lipid volume fractions respectively.

Values of the absorption coefficients for each chromophore has been taken from [37]. While those values are rather definite the volume fractions and saturation varies a lot between tissue types and also between individuals. With some inspiration from [38] values for a soft tissue was chosen as

$$B = 0.04 \qquad S = 0.7 \qquad W = 0.7 \qquad L = 0.1.$$

The corresponding total absorption coefficient for this tissue is shown in figure 2.1.

2.4.2 Scattering

Scattering of light in tissue occurs mainly due to interactions with large particles (large compared to the wavelength of the light), known as Mie scattering and by refractive index mismatches at interfaces. Analogously to the absorption coefficient the scattering coefficient μ_s is defined as the average number of scattering events per unit length.

It is however not enough to characterize the frequency of scattering events, the change in direction must also be described. This is done with the scattering phase function $p(\boldsymbol{s}', \boldsymbol{s})$, which describes the probability of a photon scattering from direction $\boldsymbol{s}'$ to $\boldsymbol{s}$.

The true scattering phase function of a material is usually unknown, but it is often assumed that it only depends on the angle between $\boldsymbol{s}'$ and $\boldsymbol{s}$. In these cases it is common to assume that scattering phase function is well-approximated by the Henyey-Greenstein phase function [39]

$$p_{HG}(\boldsymbol{s}', \boldsymbol{s}) = \frac{1}{4\pi} \frac{1 - g^2}{(1 + g^2 - 2g(\boldsymbol{s}' \cdot \boldsymbol{s}))^{\frac{3}{2}}}. \tag{2.18}$$

Which depends on the parameter g known as the anisotropy factor. The anisotropy factor is the mean of the cosine over the true scattering phase function

$$g = \int_{4\pi} \int_{4\pi} \boldsymbol{s} \cdot \boldsymbol{s}' p(\boldsymbol{s}, \boldsymbol{s}') \, d\boldsymbol{s} \, d\boldsymbol{s}', \tag{2.19}$$

and is thus a number in the range [-1,1]. Values close to 1 indicates that the material is forward scattering, values close to 0 that the material is close to isotropic and values close to -1 that the material is backwards scattering.

Instead of μ_s it is common to use the reduced scattering coefficient $\mu_s' = \mu_s(1 - g)$. Employing the theory of Mie scattering μ_s' can be modelled as

$$\mu_s'(\lambda) = a \left(\frac{\lambda}{\lambda_0} \right)^{-b}, \tag{2.20}$$

where λ_0 is some reference wavelength of choice. With this construction a should be chosen as $\mu_s'(\lambda_0)$ and b, sometimes referred to as the scattering power, describes the size distribution of the scattering particles.

Values for a and b in a soft tissue has, with inspiration from [38], been chosen as

$$a = 1.5 \text{ mm}^{-1} \qquad b = 1.2$$

16

for $\lambda_0 = 500$ nm. The reduced scattering coefficient calculated with this model is shown in figure 2.1. Biological tissue is typically strongly forward scattering and the anisotropy factor for the soft tissue was chosen as $g = 0.95$. In general g might be wavelength dependant, but has for simplicity been considered constant in this case.
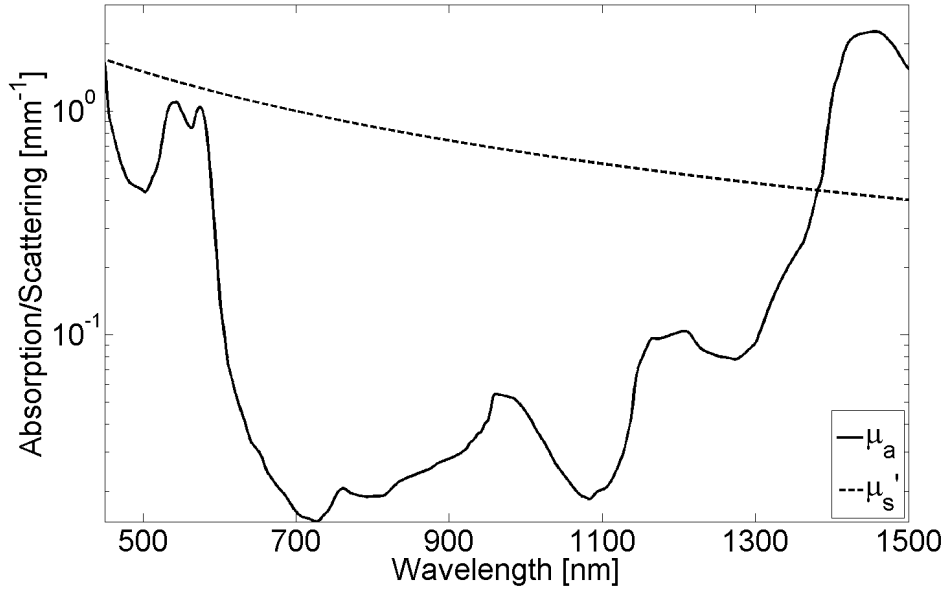
Absorption and scattering coefficients for a soft tissue

Figure 2.1: Optical properties used to model a soft tissue. Note that it is the reduced scattering coefficient μ_s' which is shown.

2.4.3 Radiative transport

The transport of photons in a turbid media, such as tissue, is described by the radiative transport equation (RTE). The time resolved RTE is a balance equation which governs the radiance at a point r in direction s with wavelength λ at a given time t, $L(r, s, \lambda, t)$. The radiance is a measure of the light intensity in units of power per area per solid angle.

The equation is deduced by considering a small volume V with boundary ∂V. The total change in radiance in V over a short time interval is then

$$\int_V \frac{\partial L}{\partial t} \, dV,$$

17

which will be equal to the difference between radiance gained and radiance lost in direction s inside of V. Radiance is gained from sources Q within V and by scattering from directions $\hat{s}'$ onto $\hat{s}$

$$\underbrace{\int_V Q \, dV}_{\text{Sources}} + \underbrace{\int_V c' \mu_s \int_{4\pi} p(s', s) L \, ds' \, dV}_{\text{Scattering onto } s} .$$

Here c' is the speed of light in the medium and $p(s', s)$ is the scattering phase function. Radiance is lost through absorption and scattering

$$-\underbrace{\int_V c' \mu_a L \, dV}_{\text{Absorption}} - \underbrace{\int_V c' \mu_s L \, dV}_{\text{Scattering}} .$$

Radiance may also be gained or lost by crossing the boundary ∂V. For an outwards pointing normal vector n of unit length this term is

$$-\underbrace{\int_{\partial V} c' s \cdot n L \, dS}_{\text{Crossing of } \partial V} .$$

By adding up these terms and dropping the volume integral, the time resolved RTE is found as

$$\frac{\partial L}{\partial t} = Q + c' \mu_s \int_{4\pi} p(s', s) L \, ds' - c'(\mu_a + \mu_s) L - c' s \cdot \nabla L. \qquad (2.21)$$

For CLI purposes the radiance is often assumed to vary slowly compared to the time required for measurements. In this case it is thus preferable to work with the stationary RTE, given by

$$0 = Q + c' \mu_s \int_{4\pi} p(s', s) L \, ds' - c'(\mu_a + \mu_s) L - c' s \cdot \nabla L. \qquad (2.22)$$

Often the directional dependence of the radiance is of little interest and instead the fluence rate Φ is used, which is defined as

$$\Phi = \int_{4\pi} L \, ds. \qquad (2.23)$$

2.4.4 Boundaries

The geometry considered in image applications is typically a subject Γ with a boundary $\partial\Gamma$ surrounded by an infinite media. The surrounding media is often air and is then assumed to behave like vacuum, i.e no scattering or absorption and with unit refractive index. All sources are assumed to be contained within Γ, this assumption is not always true, e.g in fluorescence imaging the excitation light often originates from external sources. In the case of CLI it is however valid as Cerenkov radiation can only be produced inside the subject where the refractive index is greater than unity. The light propagation in the interior of Γ is given by 2.22, but the behaviour on the boundary $\partial\Gamma$ must still be described.

Photons reaching the boundary $\partial\Gamma$, travelling in direction $\boldsymbol{s}$, will either leave Γ or be reflected back into Γ. The probability of reflection, R, is given by Fresnel's equations

$$R(\cos\varphi) = \begin{cases} \dfrac{1}{2}\left[\left(\dfrac{n_\Gamma\cos\varphi' - n_0\cos\varphi}{n_\Gamma\cos\varphi' + n_0\cos\varphi}\right)^2 + \left(\dfrac{n_\Gamma\cos\varphi - n_0\cos\varphi'}{n_\Gamma\cos\varphi + n_0\cos\varphi'}\right)^2\right] & \varphi < \varphi_c, \\ 1 & \varphi \geqslant \varphi_c. \end{cases}$$
$$(2.24)$$

Here φ is the incident angle, satisfying $\cos\varphi = \boldsymbol{s}\cdot\boldsymbol{n}$ where $\boldsymbol{n}$ is an outwards directed unit normal vector. The transmission angle φ' is given by Snell's law

$$n_0\sin\varphi' = n_\Gamma\sin\varphi, \qquad (2.25)$$

and φ_c is the critical angle for total internal reflection satisfying $n_\Gamma\sin\varphi_c = n_0$. The new direction $\boldsymbol{s}'$ of the reflected photons will satisfy

$$\boldsymbol{s} = \boldsymbol{s}' - 2(\boldsymbol{s}'\cdot\boldsymbol{n})\boldsymbol{n}. \qquad (2.26)$$

The other possible source of boundary photons directed into Γ is a boundary source, adding these together the partially reflecting boundary condition is found as

$$L(\boldsymbol{r},\boldsymbol{s}') = Q(\boldsymbol{r},\boldsymbol{s}') + R(\boldsymbol{s}\cdot\boldsymbol{n})L(\boldsymbol{r},\boldsymbol{s}), \quad \boldsymbol{r}\in\partial\Gamma, \quad \boldsymbol{s}'\cdot\boldsymbol{n} < 0, \qquad (2.27)$$

where $\boldsymbol{s}$ is given by 2.26.

2.4.5 Detection

Photons crossing the boundary $\partial\Gamma$ can be detected with an external light sensitive device. While interior detection is possible it is not common in the field of molecular imaging and will not be considered in this work. The scored quantity of these measurements are the exiting partial currents J^+ of photons at the boundary, which is given by

$$J^+(\boldsymbol{r}) = \int\limits_{\boldsymbol{s}\cdot\boldsymbol{n}>0} [1 - R(\boldsymbol{s}\cdot\boldsymbol{n})]\, L(\boldsymbol{r}, \boldsymbol{s})\boldsymbol{s}\cdot\boldsymbol{n}\, d\boldsymbol{s}. \tag{2.28}$$

The actual measurement also depends on the device used as all photons reaching the detector wont be registered. This is described by the camera's quantum efficiency (QE) is the ratio of detected photons to total photons entering the aperture. The quantum efficiency is generally wavelength dependent and varies between devices.

The measurements M will be proportional to

$$M(\boldsymbol{r}, \lambda) \propto \text{QE}(\lambda)\, J^+(\boldsymbol{r}, \lambda) \tag{2.29}$$

if the device is spectrally resolved, otherwise

$$M(\boldsymbol{r}) \propto \int_{\text{QE}>0} \text{QE}(\lambda)\, J^+(\boldsymbol{r}, \lambda)\, d\lambda. \tag{2.30}$$

Most detection devices operate by converting detected light to electrical currents. The measured values will thus not be in any ordinary units of light intensity. The relationship between incoming light and pixel values should however be linear. The measurements can thus be converted back to any intensity unit of choice by multiplication with a calibrating factor. This calibration factor is commonly found experimentally by measuring some well defined amount of light.

2.4.6 The simplified spherical harmonics approximation

Solutions to the RTE are notoriously hard to calculate, especially in more complex geometries. For this reason numerous methods to approximate it has been developed. The most widely used is the diffusion approximation, which belongs to a family of methods known as the spherical harmonics approximations, often abbreviated P_N. These are found by expanding L into a series of spherical harmonics, which results in a set of coupled partial differential equations. The popularity of the diffusion approximation is much due to it reducing down to a single, rather

20

simple equation. The simplicity of it comes at the cost of some rather strong assumption which limits its validity regions where the light is diffuse. This limits its use to media where $\mu_a \ll \mu_s'$ and to regions sufficiently far away from anisotropic sources. To overcome these limitations higher order approximations can be used, the complexity of the P_N methods does however increase rapidly with the order.

As an alternative to the complicated high order P_N equations the simplified spherical harmonics, denoted SP_N, was developed. The first order SP_1 and P_1 methods are both equivalent to the diffusion approximation. For higher orders the SP_N methods are however, as the name suggests, simpler than the P_N methods. The SP_N approximation in three dimensions was originally deduced from the P_N equations in one dimension by simply interchanging the spatial derivative with the gradient

$$\frac{\partial}{\partial x} \to \nabla.$$

For odd orders N this yields a system of $k = \dfrac{N+1}{2}$ coupled partial differential equations

$$-\nabla \cdot \boldsymbol{D}\nabla\boldsymbol{\varphi} = \boldsymbol{\nu}Q + \boldsymbol{\Lambda}\boldsymbol{\varphi}, \tag{2.31}$$

where

$$\boldsymbol{D} = \begin{pmatrix} D_1 & & \mathbf{0} \\ & \ddots & \\ \mathbf{0} & & D_k \end{pmatrix} \quad \boldsymbol{\varphi} = \begin{bmatrix} \varphi_1 \\ \vdots \\ \varphi_k \end{bmatrix} \quad \boldsymbol{\nu} = \begin{bmatrix} \nu_1 \\ \vdots \\ \nu_k \end{bmatrix} \quad \boldsymbol{\Lambda} = \begin{pmatrix} \Lambda_{1,1} & \dots & \Lambda_{1,k} \\ \vdots & \ddots & \vdots \\ \Lambda_{k,1} & \dots & \Lambda_{k,k} \end{pmatrix}$$

which is a set of diffusion-like equations without any cross-terms [40]. Here φ_i denotes the ith composite Legendre moment of the radiance and D_i, ν_i and $\Lambda_{i,j}$ are coefficients depending on the optical parameters μ_a, μ_s and g. From the composite Legendre moments the radiance can be recovered as the linear combination

$$L = \boldsymbol{\nu}^T\boldsymbol{\varphi}. \tag{2.32}$$

While this approach resulted in fewer and simpler equations than the P_N approximation, the original deduction was theoretically weak and was therefore not widely employed. A more rigorous theory for the method was however presented in the 90s showing that the SP_N equations produce solutions similar to the P_N method [41–43]. With this theory the SP_N methods gained interest and has since been used in a variety of applications, including CLI [44].

2.5 Inverse problem

So far the propagation of light in a subject from a given source has been described, which is commonly referred to as the forward problem. In optical imaging the goal is to achieve the opposite, that is to retrieve information about the source or subject given measurements of emitted radiation. This is usually referred to as the inverse problem. In CLI it is the activity distribution which is of interest, but in other applications it might be other quantities, e.g optical properties.

A common way to formulate an inverse model is to develop a forward model

$$\mathcal{F}(\boldsymbol{\theta}, \boldsymbol{X}) = \boldsymbol{M}, \tag{2.33}$$

where $\boldsymbol{\theta}$ contains known parameters, $\boldsymbol{X}$ contains the unknown properties and $\boldsymbol{M}$ are the predicted measurements. An estimate of the unknowns can then be found by fitting measurements to this forward model. This results in an estimate $\hat{\boldsymbol{X}}$ which minimizes the difference between measurement $\boldsymbol{Y}$ and forward model

$$\hat{\boldsymbol{X}} = \min_{\boldsymbol{X}} \Omega(\boldsymbol{X}) = \min_{\boldsymbol{X}} \|\boldsymbol{Y} - \mathcal{F}(\boldsymbol{\theta}, \boldsymbol{X})\|. \tag{2.34}$$

2.5.1 Regularization

Often the forward model is not injective, at least not to numerical precision, which implies that there are different $\boldsymbol{X}$ which produces very similar output. This is problematic since 2.34 does not have a unique solution these cases. This implies that even if a solution is found, it might not be close to the actual solution. For this reason the problem needs to be regularized, which is usually performed by modifying 2.34 to

$$\hat{\boldsymbol{X}} = \min_{\boldsymbol{X}} \|\boldsymbol{Y} - \mathcal{F}(\boldsymbol{\theta}, \boldsymbol{X})\| + \lambda \|G(\boldsymbol{X})\|. \tag{2.35}$$

Here G is some function or operator which is small when $\boldsymbol{X}$ has some desirable properties and λ the regularization parameter, determining how much impact the regularization has on the optimization. The preferred properties of the solution is often that it should be smooth in some sense. Commonly an iterative scheme is employed for the optimization with a homogeneous initial guess. In each iteration the error between measurements and the output from the forward model with the current estimate of $\boldsymbol{X}$ is calculated. Based on the error and the regularization the estimate is updated, the details of this step depends on the optimization algorithm used. This is repeated until some termination criteria is fulfilled and the last estimate is returned as a solution to the inverse problem. During the iteration it
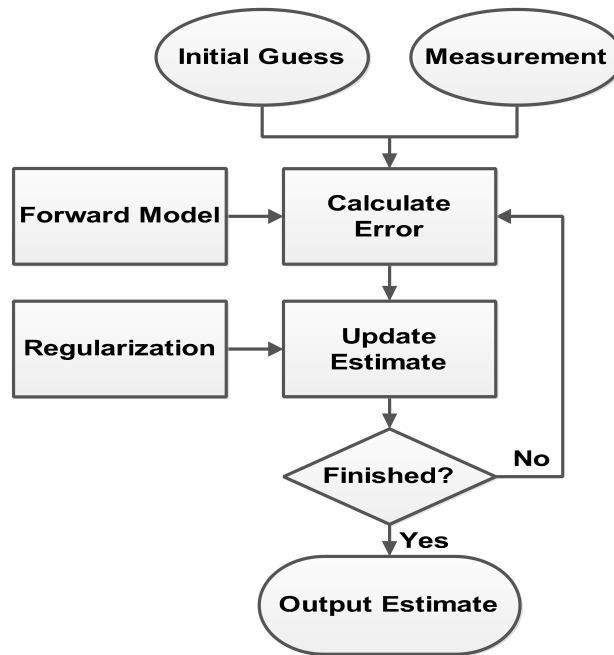
Figure 2.2: Flow chart of iterative inverse model.

is common to let the regularization parameter decrease, as a smaller value of λ brings the regularized problem 2.35 closer to the original 2.34. In 2.2 the basic outline of this type of scheme is shown.

3 METHODS

3.1 Forward model

The radiative transport equation 2.22 along with its boundary condition 2.27 and the source term 2.15 constitutes the forward model for the propagation of Cerenkov radiation. The SP_N approximation to the equation is employed but the problem is in general still not analytically solvable, thus numerical methods are required. A finite element method is employed, which transforms the model into a linear system over a discretization of the subject.

3.1.1 Discretization

The subject is discretized into N nodes, each specified by its spatial coordinates. In each node the optical properties absorption, scattering, anisotropy and refractive index are specified, allowing for both homogeneous and inhomogeneous subjects. In this way the geometry and optical characteristics of the subject is given. The activity distribution is also specified in each of the nodes. Furthermore boundary nodes can be flagged as detector nodes, specifying that the calculated intensity in these nodes should be extracted as measurements.

As a FEM approach is chosen the subject must also be divided into small elements, this is performed by a tetrahedral triangulation of the nodes. This triangulation can be performed in numerous ways, in this case a Delaunay triangulation has been chosen. This method guarantees that no nodes will reside in the interior of any circumsphere to the elements, which will limit the amount of skinny tetrahedrons. Nodes belonging to the same element will be referred to as neighbouring nodes.

The FEM discretization of 2.31 yields a system of $kN \times kN$ linear equations

$$A^k \Phi^k = q^k, \tag{3.1}$$

where once again

$$k = \frac{SP_N \text{ order } + 1}{2}.$$

Here Φ^k is the discretization of the composite Legendre moments for the fluence rate, q^k is the source vector and A^k the stiffness matrix. As the Cerenkov source is assumed to be isotropic the solution to 2.31 will also be isotropic, therefore the fluence rate can be used instead of the radiance. From the composite moments the actual fluence is recovered equivalently as radiance from the linear combination

2.32. The source vector is given by

$$q^k = \begin{bmatrix} \nu_1 q \\ \vdots \\ \nu_k q \end{bmatrix}, \tag{3.2}$$

where q is the discrete Cerenkov source vector, i.e the vector containing the Cerenkov source in each node.

To calculate the Cerenkov radiation a spectral band needs to be specified. In the implementation several spectral bands may be specified, and the the fluence rate in each of them will be separately calculated. Optical properties must be constant within each spectral band and the spectral bands must thus be chosen to accurately represent eventual wavelength dependencies.

3.1.2 Implementation

In order to solve 3.1 for Φ^k the stiffness matrix A^k and the source q^k must be found. The stiffness matrix has been calculated using the NIRFAST software. NIRFAST is an open source toolbox for Matlab with routines for modelling of optical light propagation in turbid media [45, 46]. NIRFAST provides methods to generate stiffness matrices for the $SP_1 - SP_7$ approximations.

A discrete version of the source in node i is, adopting earlier notation,

$$q_i = \sum_{j=1}^{N} \frac{1}{4\pi} \frac{1}{\Delta V_j} \int_{a_i^j}^{b_i^j} \mathbb{E}[E(r)] \, dr A_j \Delta \boldsymbol{r}'_j. \tag{3.3}$$

Here a_i^j and b_i^j are some distances between which the Cerenkov radiation produced from decays in node j is considered to belong to node i. The volume elements ΔV_j and $\Delta \boldsymbol{r}'_j$ both describe the volume which node j represents and they will thus cancel out. Finally A_j is the activity density in node j. The distances has been modelled as

$$a_i^j = d_i^j - \frac{\Delta r_i}{2} \quad b_i^j = d_i^j + \frac{\Delta r_i}{2}, \tag{3.4}$$

where d_i^j is the distance between node i and j and Δr_i is some distance related to the density of nodes in the vicinity of node i. The integral in 3.3 is further approximated by

$$\int_{d_i^j - \frac{\Delta r_i}{2}}^{d_i^j - \frac{\Delta r_i}{2}} \mathbb{E}[E(|r|)] \, dr \approx \mathbb{E}[E(d_i^j)] \Delta r_i. \tag{3.5}$$

Inserting this approximation back into 3.3 yields the discrete source

$$q_i = \sum_{j=1}^{N} \frac{1}{4\pi} \mathbb{E}[E(d_i^j)] A_j \Delta r_i, \tag{3.6}$$

where $\mathbb{E}[E(d_i^j)]$ is calculated as a discrete version of 2.10

$$\mathbb{E}[E(d_i^j)] = 2\pi^2 e^2 dr \left(\frac{1}{\lambda_1^2} - \frac{1}{\lambda_2^2} \right) \sum_i \left(1 - \frac{1}{\beta(r)^2 n^2} \right) f(E_{0_i}) \Delta E_0. \tag{3.7}$$

The node distance Δr_i was chosen as the average distance between node i and its neighbouring nodes.

As the siffness matrix often is very large an iterative method is used to solve 3.1. In this implementation a preconditioned, biconjugate gradient stabilized method has been employed, with an incomplete Cholesky factorization as preconditioner.

All implementation has been performed in Matlab, with the exception of a few NIRFAST routines which are executed in C. Existing NIRFAST routines has been used where applicable, mostly methods for mesh handling, matrix generations and solution extraction. NIRFAST provides a rigorous framework for fluorescence modelling which has been used as a template for the implementation of this Cerenkov model. The outline of the forward model is presented in algorithm 1.

3.2 Inverse model

In CLI it is the activity distribution which is of interest to reconstruct. To do so the optimization approach 2.34 is adopted. In this case the variable vector $\boldsymbol{X}$ thus contains the activity density in each node, which is N unknowns. All other relevant properties are assumed to be known, and are thus all contained in $\boldsymbol{\theta}$. The measurements $\boldsymbol{Y}$ contains M measurements at given locations on the boundary of the subject in one or more spectral bands, M can thus be decomposed as

$$M = \text{ number of detector nodes} \times \text{number of spectral bands}. \tag{3.8}$$

Measurements at the same location but in different spectral bands is thus considered to be completely separate measurements.

Algorithm 1 Forward model

1: $mesh \leftarrow$ discretization of subject
2: $\mathbb{E}\big[\frac{dE}{dr}\big] \leftarrow 2\pi^2 e^2 \left(\frac{1}{\lambda_1^2} - \frac{1}{\lambda_2^2}\right) \sum_i \left(1 - \frac{1}{\beta^2 n^2}\right) f(E_{0_i})\Delta E_0$
3: $A^k \leftarrow$ generate_matrix$(mesh, k)$
4: **for** $i = 1, \ldots, N$ **do**
5:     **for** $j = 1, \ldots, N$ **do**
6:         $d_i^j \leftarrow$ distance between node i and j
7:     **end for**
8:     $\Delta r_i \leftarrow$ avarage distance between node i and its neighbours
9:     $q_i \leftarrow \sum_j \frac{1}{4\pi}\mathbb{E}\big[\frac{dE}{dr}(d_i^j)\big]A_j \Delta r_i$
10: **end for**
11: $q^k \leftarrow \begin{bmatrix} \nu_1 q^T & \ldots & \nu_k q^T \end{bmatrix}^T$
12: $P \leftarrow$ incomplete_Choleskey_factorization(A^k)
13: $\Phi^k \leftarrow$ BICGSTAB(A^k, q^k, P)
14: $\Phi \leftarrow \sum_i \nu_i \Phi_i^k$
15: $\boldsymbol{Y} \leftarrow$ extract Φ at detector nodes

3.2.1 Linearity

As earlier mentioned the Cerenkov source term depends linearly on the activity. From 2.22 it can be seen that the radiance also depends linearly on the source, which in turn implies that the radiance depends linearly in the activity. In the discrete case the forward model is a map from the N nodes onto the M measurements

$$\mathcal{F} : N \rightarrow M.$$

Since $\mathcal{F}$ depends linearly on the activity distribution $\boldsymbol{X}$ it can be expressed as

$$\mathcal{F}(\boldsymbol{X}) = J\boldsymbol{X} + \boldsymbol{C}, \tag{3.9}$$

where J is the constant $M \times N$ Jacobian matrix of $\mathcal{F}$ and $\boldsymbol{C}$ is a constant vector. Where obviously $\boldsymbol{C} = \boldsymbol{0}$ since $\boldsymbol{X} = \boldsymbol{0}$ implies zero Cerenkov emission and thus zero detection. This has the rather simple interpretation that each measurement is a weighted sum of the contributions from all nodes.

3.2.2 Minimization

The fitting error between the measurements and an activity distribution is defined as

$$\boldsymbol{\delta} = \boldsymbol{Y} - \mathcal{F}(\boldsymbol{X}), \tag{3.10}$$

and the function to minimize, ignoring regularization for the moment, is

$$\Omega = \boldsymbol{\delta}^T \boldsymbol{\delta}. \tag{3.11}$$

The first order condition for the minimization of 3.11 is

$$\frac{d\Omega(\boldsymbol{X})}{d\boldsymbol{X}} = -2J^T \boldsymbol{\delta} = 0. \tag{3.12}$$

An iterative approach is employed to find activity distributions which satisfy 3.12. The ith fitting error is

$$\boldsymbol{\delta}_i = \boldsymbol{Y} - \mathcal{F}(\boldsymbol{X}_i) = \boldsymbol{Y} - J\boldsymbol{X}_i. \tag{3.13}$$

This can be further expanded to

$$\boldsymbol{Y} - J\boldsymbol{X}_i = \boldsymbol{Y} - J\boldsymbol{X}_{i-1} - J(\boldsymbol{X}_i - \boldsymbol{X}_{i-1}) = \boldsymbol{\delta}_{i-1} - J\Delta\boldsymbol{X}_i. \tag{3.14}$$

Inserting this into 3.12 yields the update equation

$$J^T J \Delta\boldsymbol{X}_i = J^T \boldsymbol{\delta}_{i-1}, \tag{3.15}$$

from which the next estimate is found as $\boldsymbol{X}_i = \boldsymbol{X}_{i-1} + \Delta\boldsymbol{X}_i$.

3.2.3 Regularization

The matrix $J^T J$ is often poorly conditioned, causing numerical solutions of 3.15 to be inaccurate. As discussed earlier there is also often multiple solutions to it. Regularization was presented as a way of directing the optimization towards solutions with certain properties. The regularization can also stabilize the equation from a numerical point of view.

A common strategy is to start the iteration with a large λ, to force early estimates to be smooth and then gradually lower it. As λ decreases the estimates should approach a solution to 3.12 while hopefully maintaining the smoothness from the early iterations.

One way to regularize the problem is to add a diagonal matrix λI to $J^T J$, which stabilizes it since diagonally dominant matrices always are invertible. This approach results in the Levenberg-Marquardt algorithm given by the update equation

$$\left[J^T J + \lambda I\right] \Delta\boldsymbol{X}_i = J^T \boldsymbol{\delta}_{i-1}. \tag{3.16}$$

For small values of λ 3.16 behaves similarly to 3.15 and thus produces similar updates, but might still suffer the numerical instabilities. Large values of λ will on the other hand yield good numerical robustness but will typically result in a slower convergence. Another interpretation is that for small λ the algorithm behaves similarly to the Gauss-Newton algorithm and for large λ as the method of gradient descent. This further motivates an initially large regularization parameter which gradually decreases as the gradient descent will be preferable far from an optimum, early iterations, while Gauss-Newton has superior performance close to an optimum.

In terms of 2.35 this regularization is equivalent to the minimization of

$$\Omega_\lambda = \|\boldsymbol{Y} - \mathcal{F}(\boldsymbol{X})\|^2 + \lambda\|\boldsymbol{X} - \boldsymbol{X_{est}}\|^2, \qquad (3.17)$$

where $\boldsymbol{X_{est}}$ is chosen as the previous estimate of $\boldsymbol{X}$, i.e $\boldsymbol{X_{est}} = \boldsymbol{X_{i-1}}$ for all i. This regularization will thus penalize new estimates for deviate from the previous ones. While this might cause a slower rate of convergence it should result in consecutive estimates to have similar shape and smoothness. If the initial guess is smooth it is thus likely that the resulting, final estimate will be rather smooth, as often only a few iterations are performed.

The regularization parameter has been modelled as

$$\begin{aligned} \lambda_0 &= \tilde{\lambda}\max(J^T J), \\ \lambda_i &= \alpha\lambda_{i-1}, \end{aligned} \qquad (3.18)$$

which makes the new parameters less dependant on the mesh, as the factor $\max(J^T J)$ puts λ_0 in the right order of magnitude. The parameter α determines the rate at which λ decreases and should be chosen in the interval $(0, 1)$.

3.2.4   Jacobian calculation

The Jacobian J is a $M \times N$ matrix where entry i, j represents the rate if change in measurement in detector i due to a unit increase of activity in node j. Classically the perturbation method was used to find it, which relied on the individual perturbation of each node followed by solving the forward model. For each such iteration one column of J would be found. With this approach the computation of J thus requires the forward model to be solved N times, which in most cases is computationally expensive.

A more efficient way of calculating J is by using the adjoint formulation. It is based on the principle that the fluence rate in node i due to the activity in node j should be the same as the fluence in node i due to the same activity in node j.

More simply put, a detector in node j will measure the same signal from a point activity in node i as a detector in node i would measure from a point activity in node j [47, 48].

Exploiting this the perturbation method can be employed to the detector nodes only. With this approach one row instead of a column of J is found per iteration, thus only requiring the forward model to be solved M times. The number of measurements are usually much smaller than the number of nodes and this method will thus be much more efficient the classic perturbation method.

3.2.5 Implementation

Similarly to the forward model the the inverse model has been implemented in Matlab, once again using NIRFAST's fluorescence routines as a template.

As the inverse model is based on the forward model the subject must be discretized in the same manner. The one difference is that the activity distribution, which now is unknown, is set to some initial guess. To speed up the optimization a secondary, coarser, mesh is used to calculate the updates, while the fitting errors are calculated on the original mesh.

As a measure of the progress of the optimization the relative change in squared errors between subsequent iterations

$$p_i = \frac{\boldsymbol{\delta}_{i-1}^T \boldsymbol{\delta}_{i-1} - \boldsymbol{\delta}_i^T \boldsymbol{\delta}_i}{\boldsymbol{\delta}_{i-1}^T \boldsymbol{\delta}_{i-1}} \tag{3.19}$$

is used. If $p_i < 0$ the sum of the squared errors has increased, in this case the previous estimate $\boldsymbol{X_{i-1}}$ is considered to be better than $\boldsymbol{X_i}$ and the iterations are terminated and $\boldsymbol{X_{i-1}}$ is returned. The other possibility is $0 \leqslant p_i \leqslant 1$, in this case the new estimate $\boldsymbol{X_i}$ is considered to be better than the previous one and is kept as the current estimate. However if p_i is small, below a certain threshold, it is likely that future iterations will also results in minor improvements. As the forward model has to be solved in each iteration this will result in a high computational cost for small results. For this reason the iterations are terminated if p_i is below a certain threshold. In this implementation this threshold has been chosen as 0.02.

The reconsturcion algorithm starts with the calculation of the Jacobian matrix on the fine mesh and it is then downsampled to the coarse mesh. This is only done once since J is constant. At the start of each iteration the fitting error $\boldsymbol{Y} - \mathcal{F}(\boldsymbol{X}_i)$ is calculated for the current estimate, at the first iteration the initial guess $\boldsymbol{X}_0$ is used. After the error is found p_i is calculated and the termination criteria are checked, this is not performed on the first iteration. If no criteria is fulfilled the

current estimate is downsampled to the coarse mesh and updated accordingly to 3.16. The new estimate is interpolated back to the fine mesh and the next iteration is initiated, unless the iteration limit is reached. The inverse model is summarized in algorithm 2.

Algorithm 2 Reconstruction scheme

1: $J \leftarrow \dfrac{d\mathcal{F}}{d\boldsymbol{X}}$

2: $J_C \leftarrow$ downsample J onto coarse mesh

3: $\lambda \leftarrow \tilde{\lambda} \max(J_C^T J_C)$

4: $i \leftarrow 1$

5: **while** $i \leqslant$ Iterations **do**

6:      $\boldsymbol{\delta}_i \leftarrow \boldsymbol{Y} - \mathcal{F}(\boldsymbol{X}_i)$

7:      **if** $i > 1$ **then**

8:          $p_i \leftarrow \dfrac{\boldsymbol{\delta}_{i-1}^T \boldsymbol{\delta}_{i-1} - \boldsymbol{\delta}_i^T \boldsymbol{\delta}_i}{\boldsymbol{\delta}_{i-1}^T \boldsymbol{\delta}_{i-1}}$

9:          **if** $p_i < 0$ **then**

10:             **return** $\boldsymbol{X}_{i-1}$

11:          **else if** $p_i <$ tol **then**

12:             **return** $\boldsymbol{X}_i$

13:          **end if**

14:          $\lambda \leftarrow \alpha\lambda$

15:      **end if**

16:      $\boldsymbol{X}_i^C \leftarrow$ downsample $\boldsymbol{X}_i$ onto coarse mesh

17:      $H \leftarrow J_C^T J_C + \lambda I$

18:      $\Delta \boldsymbol{X}_{i+1}^C \leftarrow H^{-1} J^T \boldsymbol{\delta}_i$

19:      $\boldsymbol{X}_{i+1}^C \leftarrow \boldsymbol{X}_i^C + \Delta \boldsymbol{X}_{i+1}^C$

20:      $\boldsymbol{X}_{i+1} \leftarrow$ interpolate $\boldsymbol{X}_{i+1}^C$ onto fine mesh

21:      $i \leftarrow i + 1$

22: **end while**

3.2.6 Post processing

Depending on the application it may be preferable to further process the reconstructed activity $\hat{\boldsymbol{X}}$. If the activity is expected to be distributed smoothly over a volume a smoothing filter might be useful. If, on the other hand, the activity is expected to be very localized such filtering might not be suitable.

The estimate will typically contain a non-zero activity in each node, however often many of the values will be very small. These values are rarely of interest and will often considered as nodes with zero activity. For this reason it is often suitable to threshold the data

$$\hat{\boldsymbol{X}}_T(i) = \begin{cases} \hat{\boldsymbol{X}}(i) & \hat{\boldsymbol{X}}(i) > T \\ 0 & \hat{\boldsymbol{X}}(i) \leqslant T. \end{cases} \tag{3.20}$$

Although these values are rather insignificant individually, summed up they might still constitute a significant fraction of the total reconstructed activity. For quantitative measurements this must be considered. One way of dealing with this is to scale the thresholded data so that it contains the same total activity as the original estimate

$$\hat{\boldsymbol{X}}_T^* = \frac{\sum \hat{\boldsymbol{X}}}{\sum \hat{\boldsymbol{X}}_T} \hat{\boldsymbol{X}}_T. \tag{3.21}$$

3.2.7 Hybrid reconstruction scheme

For reconstruction measurements in multiple spectral bands are often preferable to a single one. This will however often require multiple measurements and additional equipment. In some cases data might thus be limited to a single, often rather large, spectral band. Reconstructions based on such a measurement might perform poorly due to the inaccurate representation of the wavelength dependent properties.

To improve performance in these cases a hybrid multi-spectral reconstruction algorithm was implemented. In this hybrid model the measurement in the single spectral band is assumed to be a sum of the emission of several smaller spectral bands. These spectral bands are used in the forward model and the results from each band is then summed form the predicted fluence rate in the original large spectral band. In this way the wavelength dependence of the optical properties are represented during the reconstruction.

3.3 Validation

As several assumptions and approximations are used to formulate the models it is important to verify them.

3.3.1 Continuous slowing down approximation

As earlier mentioned the deceleration of β-particles in a medium is stochastic. In this model the continuous slowing down approximation is used which is a an attempt to describe the average behaviour. It is a well known fact that in general

$$f(\mathbb{E}[X]) \neq \mathbb{E}[f(X)]$$

if f is non-linear. This is relevant since the CSDA basically yields the expected value of the velocity and the amount of Cerenkov radiation emitted depends non-linearly on it. It is thus not certain that the CSDA plugged into the Frank-Tamm theory yields accurate results.

To verify the validity of this assumption the results from the CSDA were compared to a Monte Carlo simulation of electron transport. More importantly the Cerenkov radiation calculated with both methods was compared. The comparison where made in the case of a singe point of activity within an infinite medium. The Monte Carlo simulation takes more interactions into account than the CSDA. It also accounts for the scattering of the β-particles and is considered a very accurate model.

The idea of a hybrid model was presented by Hu *et al.* [7]. In their study it was concluded the its performance was shown comparable to a multi-spectral model.

3.3.2 NIRFAST SP_N

The SP_N approximations are known to be corrections to the well-established diffusion approximation. In cases where the diffusion approximation works well it is thus fair to assume that higher order SP_N methods also should perform well. In these cases higher order methods are not really of interest as the diffusion approximation will be preferable due to lower computational cost. In cases where the diffusion model does not hold it is however of interest to assess the performance of higher order methods. In order to determine which approximation to use a comparison between the $SP_1 - SP_7$ methods and Monte Carlo simulations for different optical properties was performed.

The setting of the simulation was a single, isotropic, point source in an infinite medium with constant optical properties. The simulations were performed with

μ_a ranging from 0.001-0.16 mm^{-1} and μ_s ranging from 20-60 mm^{-1} while the anisotropy factor was kept constant at $g = 0.95$. Another reason for this validation was to verify NIRFAST's implementation.

3.3.3 Forward model

One of the main goals with this work was to present a forward model for the propagation of Cerenkov radiation. A forward model has been presented but it has to be verified to see that it actually describes the propagation of Cerenkov radiation.

Two types of validation were performed for the forward model. The spectra of the emitted Cerenkov radiation from subjects with known expected outcomes were simulated. This was done for a completely transparent subject where the inherent Cerenkov spectrum, λ^{-3} is expected and in a soft tissue subject. The other validation was an attempt to recreate the experimental measurements from phantoms measurements.

3.3.4 Inverse model

The inverse model presented is basically a fitting of the forward model to measured data. The performance of the inverse model will thus heavily depend on the accuracy of the forward model. The other part of the inverse model is the optimization algorithm and the regularization, which both impacts the results.

Reconstructions has been performed on simulated data, where measurements were generated as

$$\boldsymbol{Y} = \mathcal{F}(\boldsymbol{X})$$

for an activity distribution of choice. In this case the subject was chosen as a $2 \times 2 \times 2$ cm cube with the soft-tissue properties given by figure 2.1. The activity distribution was chosen as a sphere with radius 3 mm with its center located 5 mm from the centre of one of the subjects sides.

Reconstruction was also performed on data from an *in vitro* phantom measurement. The purpose of these tests were to show the potential of the models and no quantification of their accuracy has been attempted.

To assess the performance of the optimization the absolute relative error

$$\varepsilon = \frac{|\boldsymbol{Y} - \mathcal{F}(\hat{\boldsymbol{X}})|}{\boldsymbol{Y}} \tag{3.22}$$

was considered. As this is a vector valued quantity its mean, ε_{mean}, and maximum value, ε_{max}, were chosen to represent it.

3.4 Experimental set-up and equipment

An *in vitro* study was conducted to test the performance of the presented models.

3.4.1 Phantoms

For the *in vitro* studies block shaped phantoms measuring $9 \times 3 \times 2$ cm were used. The phantoms were made out of epoxy resin. In order to cause the phantoms to scatter light different concentrations of TiO_2 were mixed in, as well as toner ink for absorption. The phantoms were developed during a thesis project assessing the imaging potential of Cerenkov emission [49]. Through the phantoms holes were drilled, in which silicone tube filled with radioactive fluid was fitted, acting as the activity distribution for the measurements.

In the experiments three different phantoms where used, labelled B3, C3 and D3. They all had the same scattering properties but increasing absorption coefficients.

The optical properties of phantom B3 is shown in figure 3.1. The epoxy resin, and thus the phantoms, has a refractive index of 1.54, which will produce a stronger Cerekov emission than most tissues. The phantoms were based on the ones used in [50], where the anisotropy factor was found to be about $g = 0.75$.
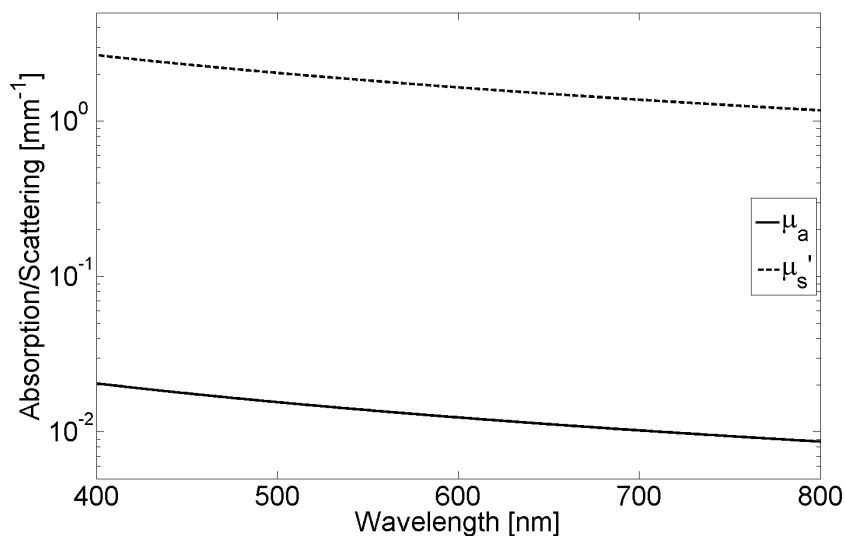
Figure 3.1: Optical properties of phantom B3. The other phantoms used, C3 and D3, had the same scattering coefficient but two and four times higher absorption respectively.

3.4.2   Radioactive isotopes

Two different β-emitting radioisotopes were used in the phantom measurements. ^{18}F, which is one of the most commonly used isotopes in PET, and ^{66}Ga. These isotopes has rather different characteristics, ^{18}F emits relatively low energy positrons and has a half-life of about 110 minutes. ^{66}Ga on the other hand emits positrons with high energies and has a half-life of roughly 9.5 hours. The energy spectrum for the two isotopes are shown in figure 3.2. From the spectra it can be seen that
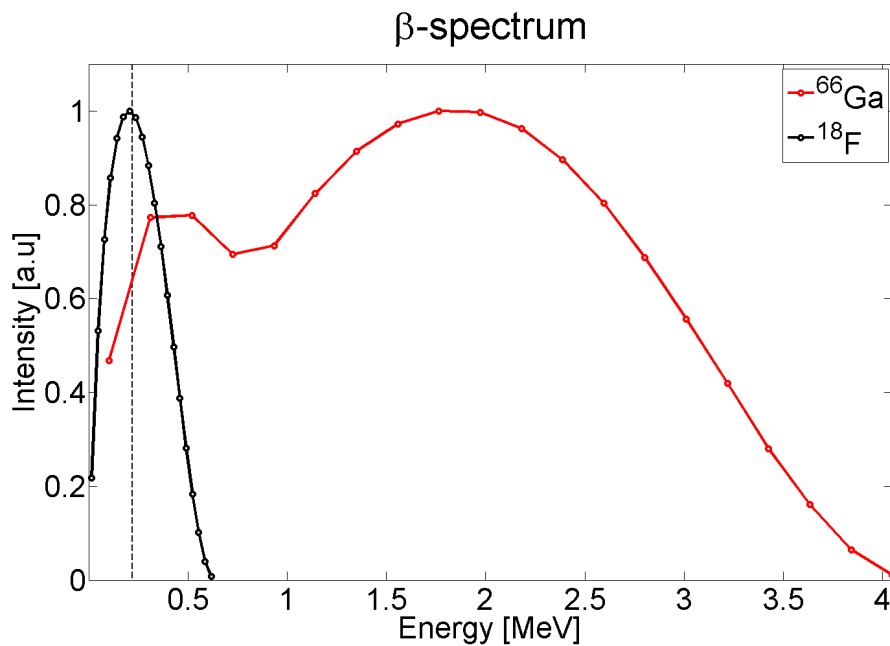
Figure 3.2: Unnormalized spectra for the energy of emitted positrons from ^{18}F and ^{66}Ga [31]. The dashed line indicated the threshold for Cerenkov emission in soft tissue.

roughly half of the decays from ^{18}F results in the emission of Cerenkov radiation while this number is significantly higher for ^{66}Ga.

From a clinical perspective ^{18}F has the nice property of delivering a rather small dose to the subject, due to its low energy emission and fast decay. ^{66}Ga will produce a strong signal over a longer period of time. Properties which could be very useful in preclinical studies.

3.4.3   Camera

The detection device used in the experimental measurements was a front illuminated Andor iKon-M 934. This is a CCD with 1024×1024 pixels of size 13×13 μm [51].

This camera was used both for the detection of Cerenkov emission and white-light images of the set-up. During measurements the camera was cooled to -85° C to reduce the influence of noise caused by dark currents.

The quantum efficiency of this camera is shown in figure 3.3. As both of the radionuclides used in the studies were positron emitters a significant amount of 511 keV gamma photons were produced from annihilations. While the camera is insensitive to these photons some of them will still be registered. These detected gamma photons will produce a very strong signal due to their very high energy.

The strongest signal in the raw image acquired will typically be the 511 keV gamma photons and in order to extract the Cerenkov emission some processing of the data is required.
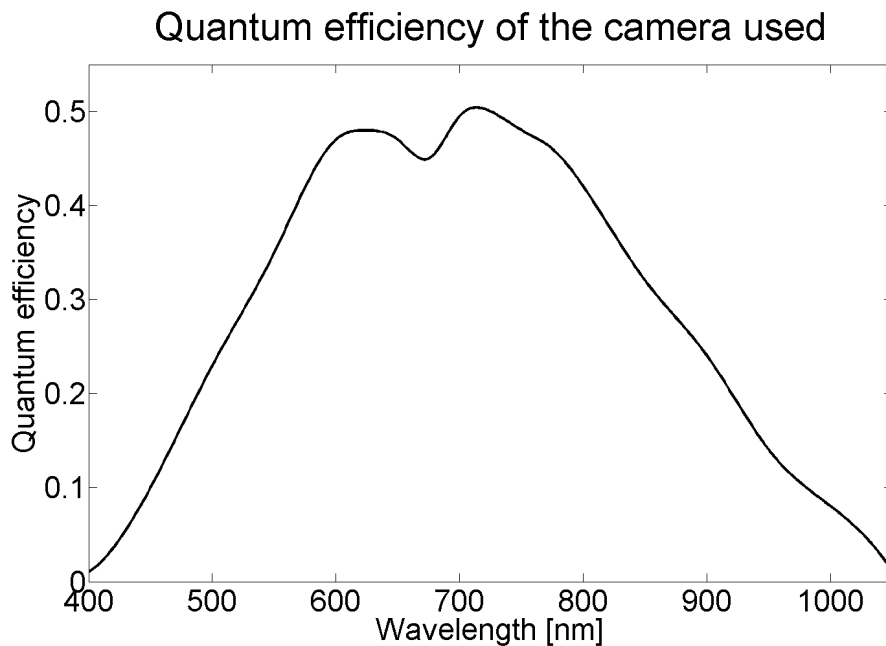
Figure 3.3: Quantum efficiency of the Andor iKon-M 934 CCD used for the measurement [51].

3.4.4 Pre-processing of measurements

To increase the sensitivity of the Cerenkov measurements the acquired image was subjected to 4×4 pixel binning in the ^{66}Ga experiment and 8×8 in the ^{18}F measurement. Following the binning a 9×9 pixel median filter was employed to remove the signal from the gamma photons.

Due to the cooling of the system the background noise in the measurements was close to constant. This constant background was subtracted from the measurement and the resulting image were normalized with the exposure time. Finally any negative pixel values resulting from the background subtraction was removed.

3.4.5 Experimental set-up

To prevent external light from polluting the measurements the phantoms were placed in a box with the camera fitted through the top. To eliminate as much light from the outside as possible the box was covered by black fabric and cardboard sheets.

Inside the box a light diode was mounted to enable white-light images to be taken of the subject after the box had been sealed. A 10 minute exposure time were used for the Cerenkov measurements.

In the ^{66}Ga experiment the three phantoms B3, C3 and D3 was placed side by side. The tube containing the ^{66}Ga was fitted through all of them at a depth of 8 mm.

In the ^{18}F experiment only phantom B3 was used. In this case the tube was located at a depth of 4.5 mm. This phantom was also imaged by a combined PET and CT scan.
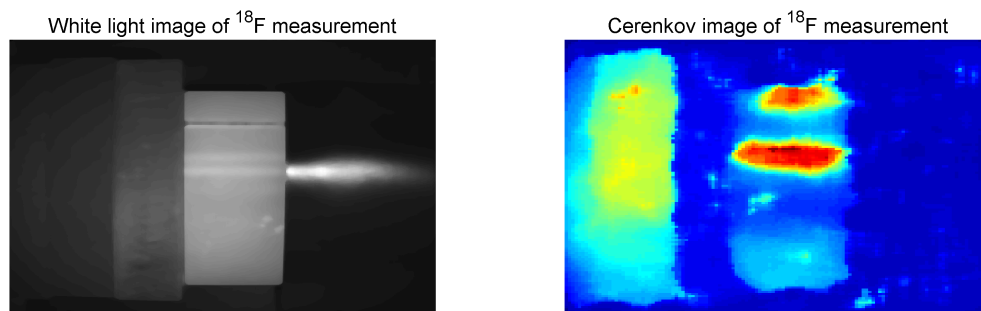
Figure 3.4: To the left, white light image of the ^{18}F experiment. To the right, the corresponding Cerenkov image of the phantom.

4 RESULTS

4.1 Continuous slowing down approximation

The Monte Carlo data for the deceleration of electrons was compared to the CSDA to verify that the stopping power used is reasonable. Calculations of the Cerenkov emission based on the two different data sets were also compared.

4.1.1 Energy distribution

The Monte Carlo simulations yielded the probability distribution of the electron energy at distances ranging from 0.1-5 mm from the decay. This distribution for electrons with an initial energy of 1 MeV is displayed in figure 4.1. On top of the distribution the results from the CSDA is plotted, and it seems to follow the high probability ridge fairly well. As the CSDA is based on the average stopping
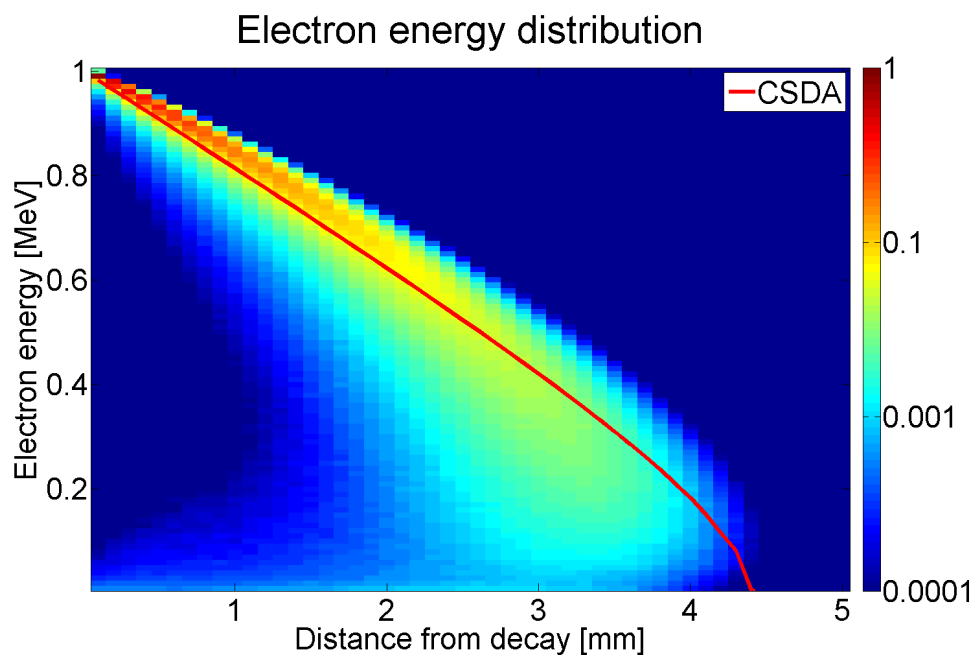
Figure 4.1: Probability distribution for 1 MeV electrons in soft tissue from the Monte Carlo simulation. Note the logarithmic scale.

power it could be of interest to see how the average electron decelerates based on the Monte Carlo distribution. This comparison is shown in figure 4.2. Clearly there are differences between the results based on the CSDA and the Monte Carlo simulation.
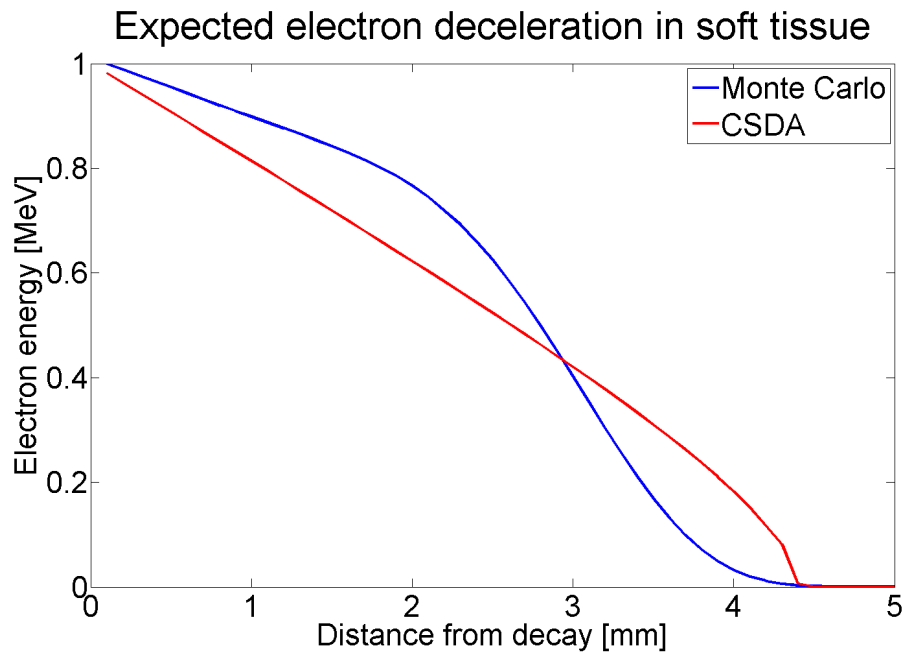
Figure 4.2: Expected electron energy versus distance travelled for 1 MeV electrons.

4.1.2 Cerenkov yield

The difference between the Monte Carlo and the CSDA data should result in some differences in the calculated Cerenkov emission. A comparison of the emitted Cerenkov radiation per path length for 1 MeV electrons is shown in figure 4.3. The differences from 4.2 seems to be well reflected in the Cerenkov emission. The total energy emitted from a 1 MeV electron, that is the integral of the curves in 4.3, is also important to compare. The total Cerenkov energy emitted from electrons with initial energy ranging from 0.1-1 MeV was compared. The results are shown in figure 4.4. Despite the differences previously seen the total energy calculated with CSDA deviates less than 5 % from the Monte Carlo calculation.
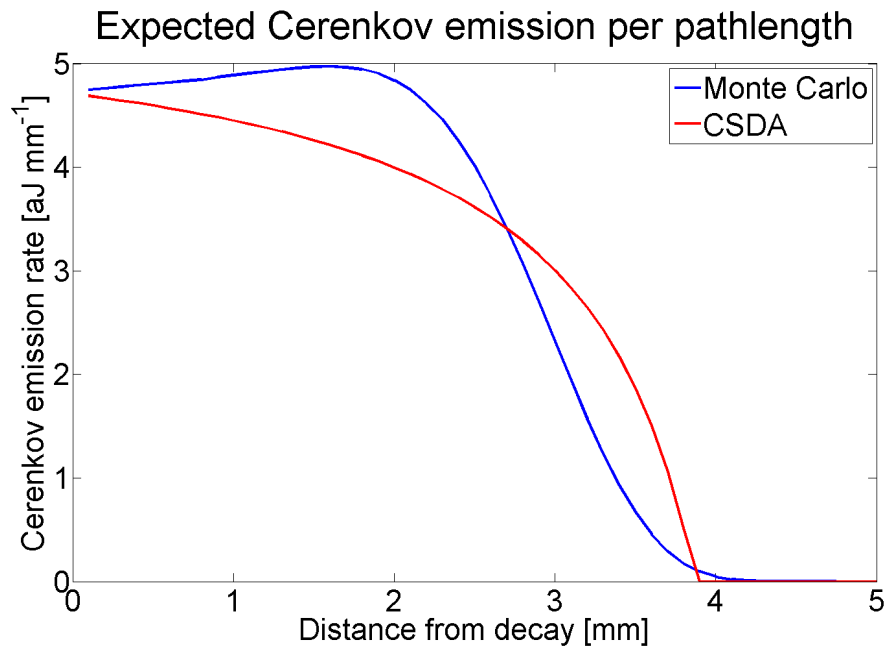
Figure 4.3: Expected Cerenkov emission per path length from 1 MeV electrons.
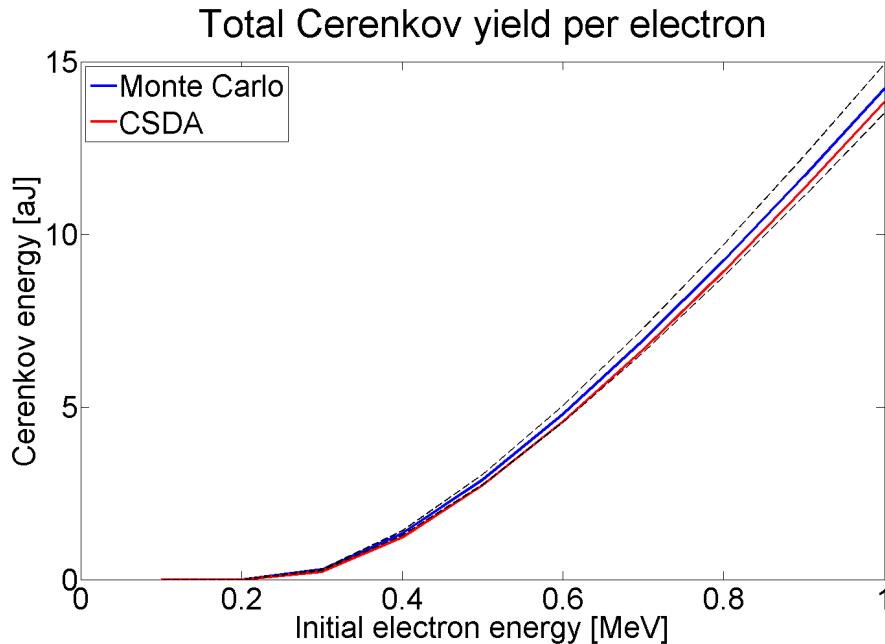
Figure 4.4: Total emitted Cerenkov radiation from electrons with initial energy ranging from 0.1-1 MeV. The dashed curves indicates the 5 % deviation region from the Monte Carlo data.

4.2 Nirfast SP_N

The results from one of the simulations comparing the SP_N methods to Monte Carlo is shown in figure 4.5. It is seen that the results from the SP_3 method be-
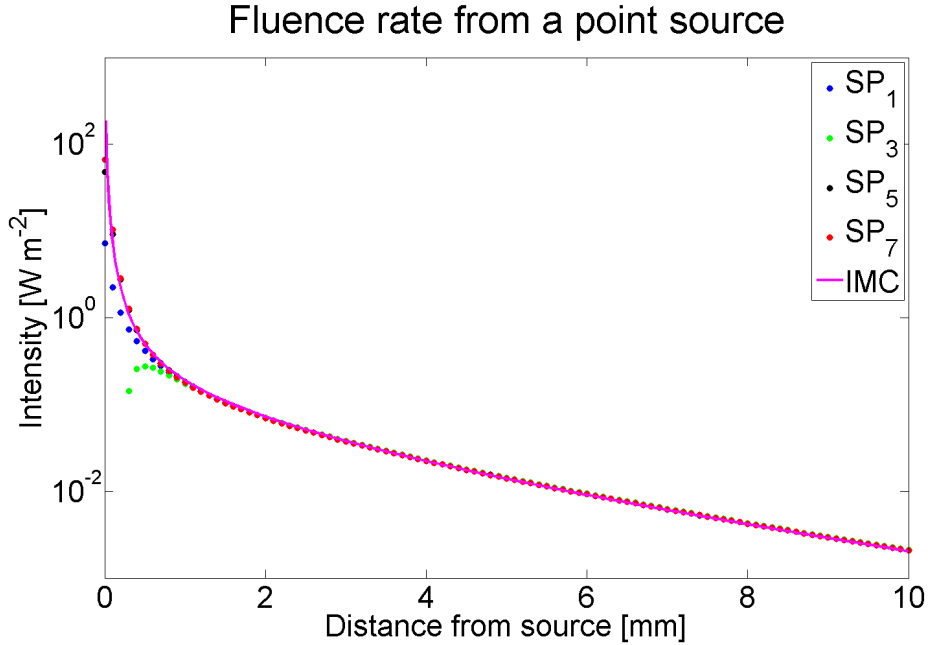

Figure 4.5: Fluence rate as a function of distance from a point source in an infinite medium. The medium has the optical properties $\mu_a = 0.02 \text{ mm}^{-1}$, $\mu_s = 20 \text{ mm}^{-1}$ and $g = 0.95$.

haves strangely close to the source, which occurred in several of the simulations. The cause for this behaviour was never isolated but numerical instabilities in the solution of 3.1 or some flaw in NIRFAST's implementation are possible explanations. Apart from this anomaly these results confirms the expected behaviour of the SP_N approximations. SP_1 does not perform as well as the higher order approximations at short distances while at longer distances all methods seem to converge.

Due to the unexpected behaviour the SP_3 method were discarded. From the simulations it was found that the SP_5 and SP_7 methods produce similar results. Since the computational cost is significantly higher for the SP_7 approximation, the SP_5 method was considered to be the better of the two.

The dependence of the performance on the optical properties for the SP_1 and SP_5 methods are shown in figure 4.6. In this figures the absolute relative error between

them and the Monte Carlo simulations are displayed at the distances 1 and 2 mm from the source. It should be noted that these plots are interpolations from only
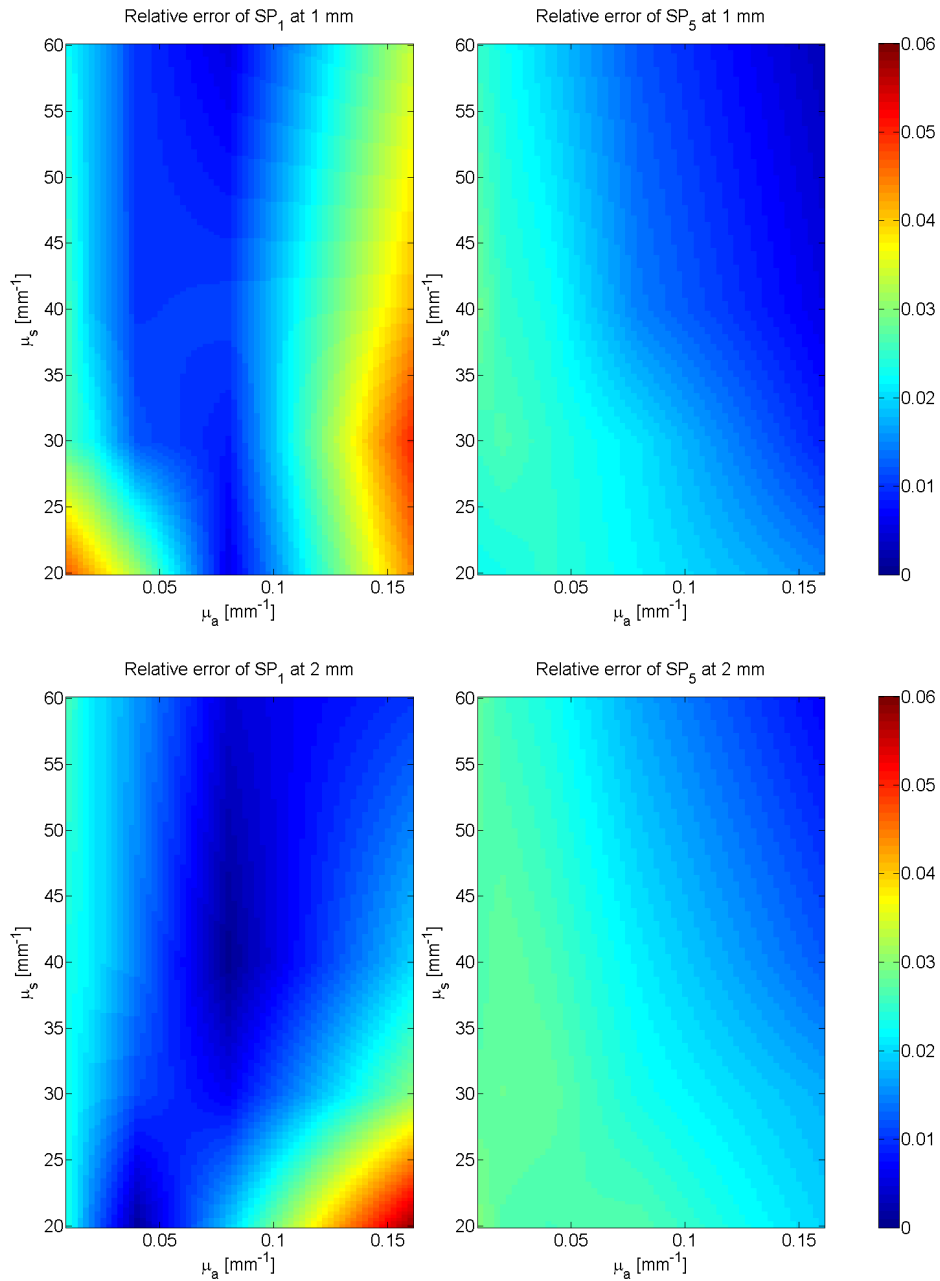

Figure 4.6: Absolute value of the relative error between SP_1, SP_5 and the Monte Carlo simulation at 1 and 2 mm distance from the source.

16 original data points. They should thus not be used to assess the error of the

43

methods for certain optical properties. The purpose of them here is to give an indication of the general behaviour of the approximations compared to a Monte Carlo simulation. In figure 4.6 it can be seen that error for SP_5 varies rather slowly and seems to follow a pattern. The error for SP_1 on the other hand is a bit erratic. At farther distances from the source the difference between SP_1 and SP_5 is small, as indicated by figure 4.5, and the corresponding plots for these distances will thus be similar.

The conclusion from these simulations are that SP_5 in general seems to produce slightly better and more consistent results than SP_1. The SP_1 method still seems fairly accurate and it is not obvious whether the extra computations required for SP_5 are worthwhile.

4.3 Forward model

The forward model was tested by simulating its spectrum in two different subjects. The emission predicted by it was also compared from the phantom experiments.

4.3.1 Simulations

The matrix generation in NIRFAST does not support completely transparent media. For the transparent simulation a close to transparent medium was used instead. This medium was chosen to have parameters $g = 1$ and $\mu_a = \mu_s = 10^{-10}$ mm^{-1}, which in practice eliminates the effects of scattering and implies an average distance between absorption events of 10^7 metres. The spectrum obtained from the forward model in this medium is shown in figure 4.7. As the absolute intensity of this spectrum is dependant on geometry, activity distribution and also on β-source the spectrum has been normalized. The spectrum calculated with the forward model matches the expected spectrum, which indicates that the Cerenkov source representation and implementation is accurate.

In the soft tissue-like medium there is no explicitly known expected spectrum to compare with. A similar simulation was performed by Spinelli *et. al* [52], and while the optical properties used in their simulation was not presented the general shape of the spectrum should be similar. The spectrum in this medium calculated with both the SP_1 and SP_5 method is shown in figure 4.8. In this simulation SP_1 and SP_5 thus produced slightly different results. The general shape of the acquired spectrum is however similar to the one presented in [52]. It also corresponds well to the absorption given in figure 2.1.

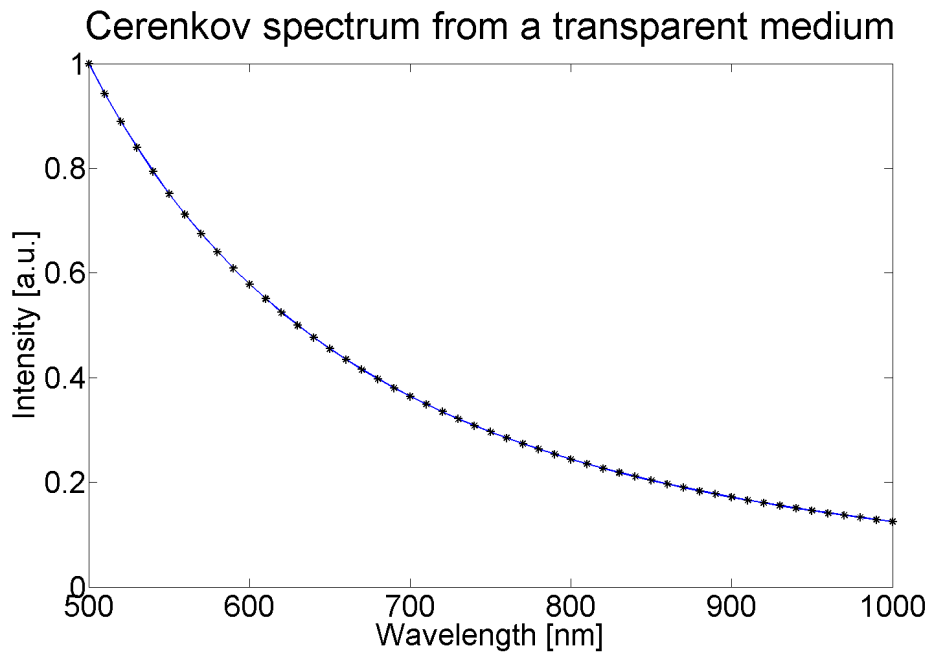## Cerenkov spectrum from a transparent medium

Figure 4.7: Normalized spectrum of the Cerenkov radiation in a transparent medium. The black dots represents the values calculated with the forward model. The solid blue curve is the expected λ^{-3} spectrum.
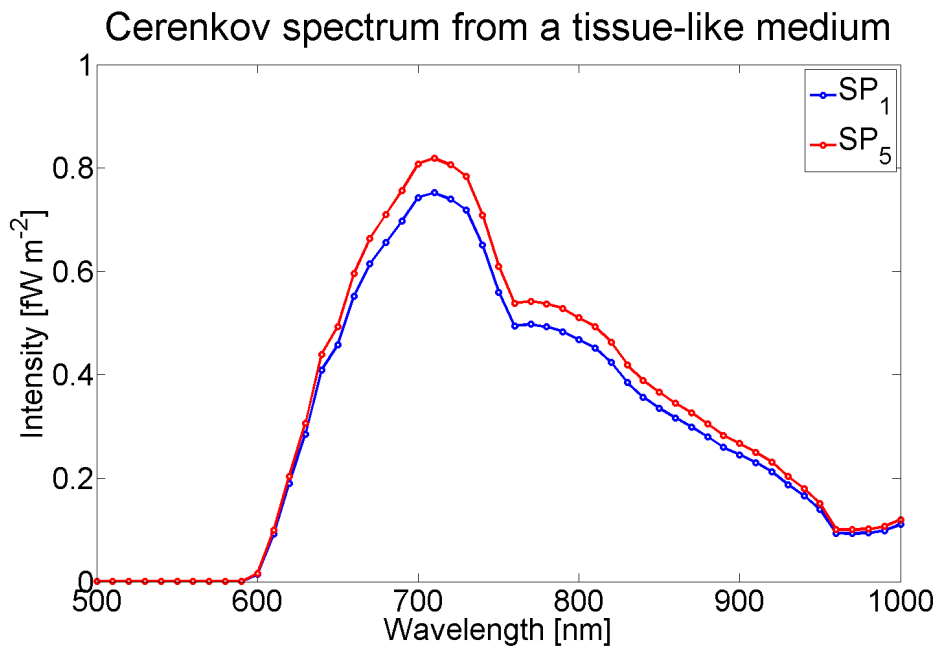
Cerenkov spectrum from a tissue-like medium

Figure 4.8: Cerenkov spectrum from a medium with soft tissue properties.

4.3.2 Experimental

The pre-processed image acquired from the ^{66}Ga phantom experiment is shown in figure 4.9 along with the forward simulation for the phantoms. The intensity
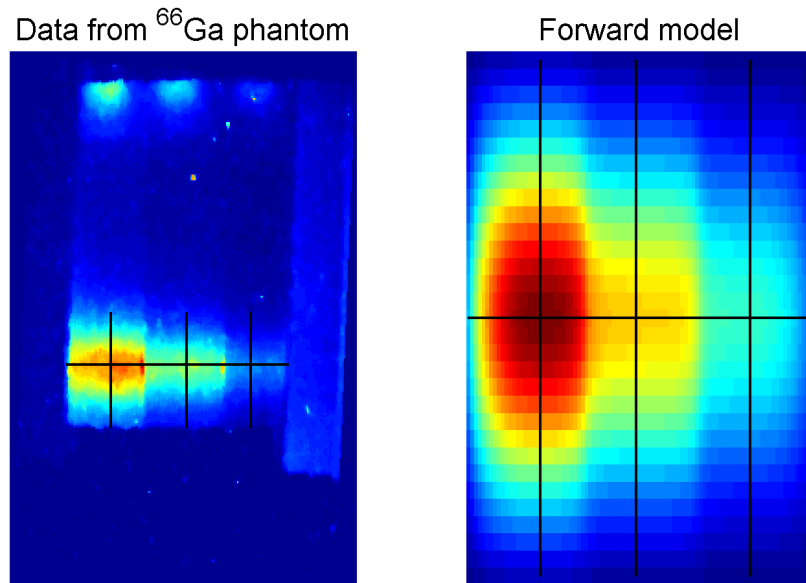

Figure 4.9: To the left, measured intensity from the ^{66}Ga phantom experiment. To the right, simulated intensity from the forward model.

was extracted along the black lines to compare the measurements to the forward model. From the extracted measured intensity outliers were removed and smoothing with a mean value filter was performed. Both intensities were normalized to have maximum value 1, the result is shown in figure 4.10. The intensities in phantoms B3 and C3 seems to be well described by the forward model while the results in D3 does not quite agree. The width profiles of the emission in the phantoms is also fairly well described by the forward model.
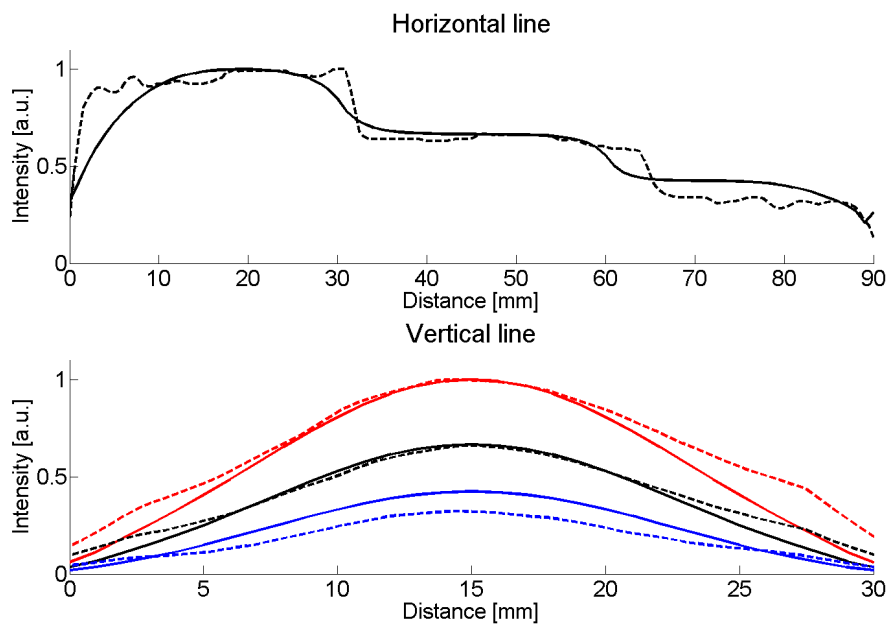
Figure 4.10: Measured and simulated intensities from the ^{66}Ga phantom experiment. Solid curves are data from the forward model and dashed curves are the measurements. In the lower plot, the red, black and blue curves are associated with phantoms B3, C3 and D3 respectively.

4.4 Inverse model

Reconstruction of the activity distribution was performed on simulated data as well as on the measurements from the ^{18}F and ^{66}Ga experiments. In the latter only phantom B3 was used as it provided the strongest signal.

4.4.1 Simulation

The subject used for the simulated reconstruction is shown in figure 4.11.
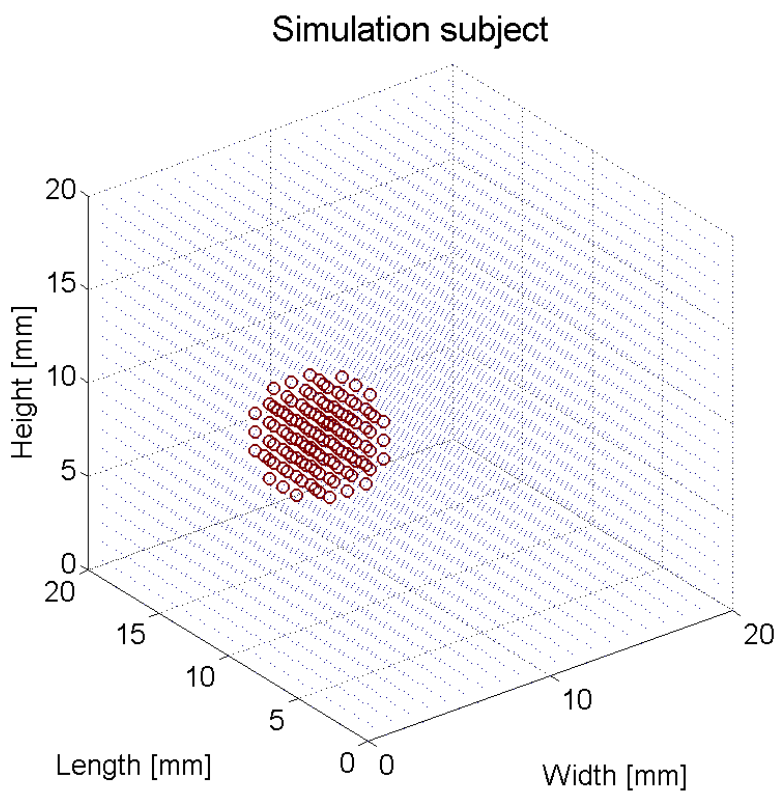

Figure 4.11: Scatter-plot of the subject used for the simulated reconstruction. The small blue dots are nodes with zero activity and the large red circles represent the spherical cluster of nodes with non-zero activity.

The reconstructed activity as well as the actual activity from the simulation along a line through the center of the sphere of activity is shown in figure 4.12. The spatial distribution of the reconstructed activity is shown in figure 4.13.
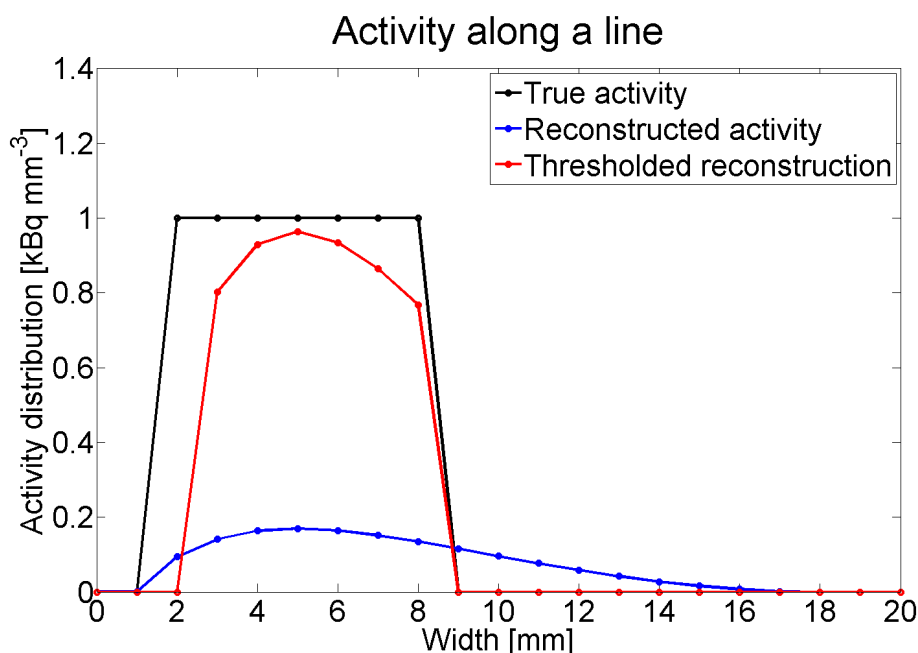
Figure 4.12: Reconstructed activity from the simulated data. The blue curve is the raw reconstructed activity, while the red curve is the reconstruction after a threshold.

The relative error of the optimization had a mean of $\varepsilon_{mean} = 2.9\ \%$ and a maximum value of $\varepsilon_{max} = 7.6\ \%$. Indicating that the reconstruction fits the measurements well.

The raw reconstructed activity produces a small fitting error, indicating that it is close to an optimum of 2.34, it is however not close to the true activity. From the results in figure 4.12 and 4.13 it is clear that the threshold can improve the reconstruction significantly. It should be noted that in this simulation the threshold was chosen to match the known activity, in a real case where the activity distribution is unknown the problem of choosing a threshold will not be so simple.

4.4.2 Experimental

As the models were not calibrated to the equipment no comparison in the absolute magnitude of the activity was possible. The measurements on the phantoms were performed without any filters and no multi-spectral data was therefore acquired. For this reason the hybrid reconstruction algorithm was used for these reconstructions.

To visualize the reconstructed activity a projection of the activity density onto the
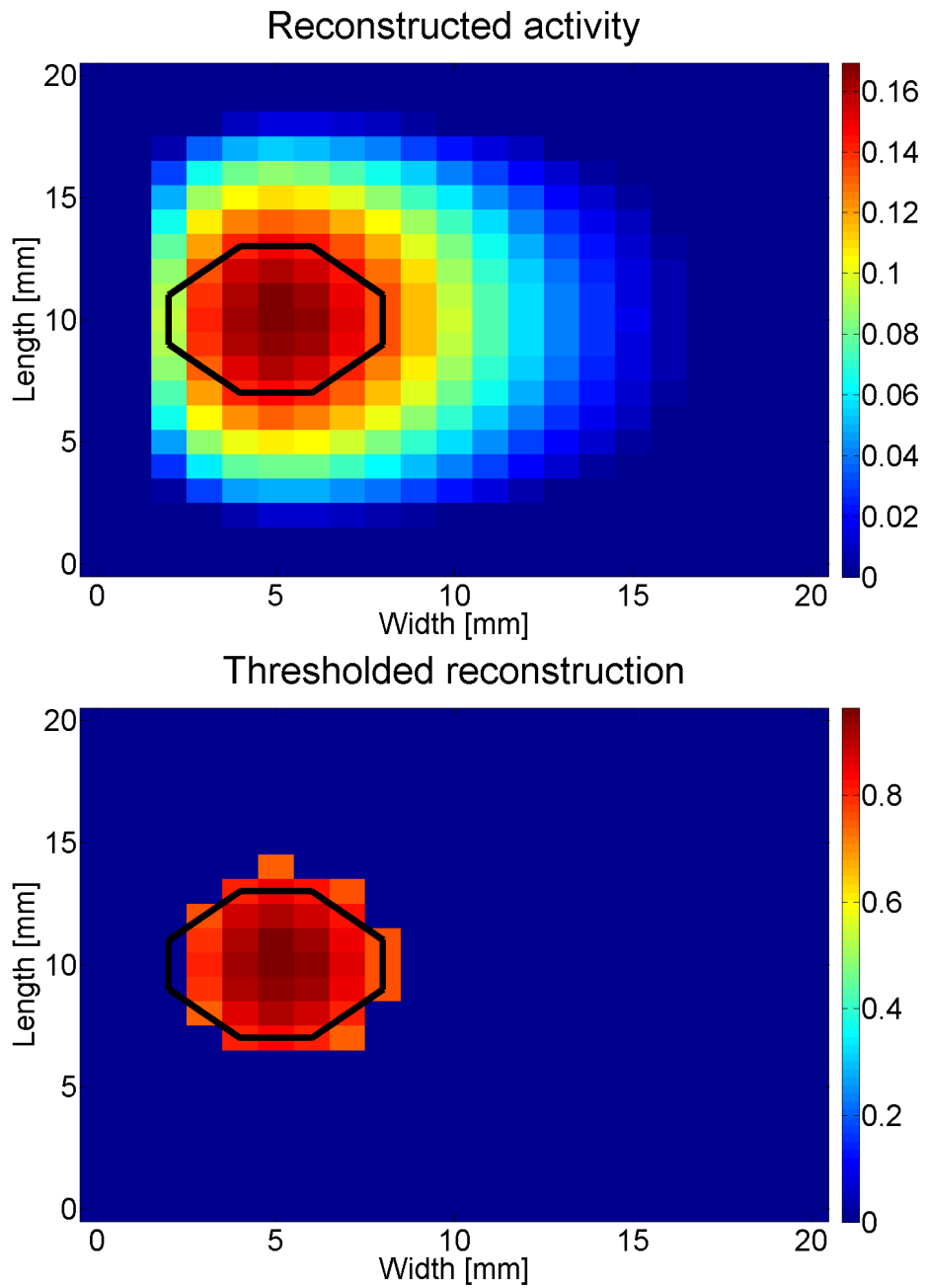
Figure 4.13: Reconstructed activity in a slice from the simulated data. The black curve indicates the boundary of the true activity distribution. The upper image displays the raw reconstructed activity and the bottom one the reconstruction after the threshold.

sides of the phantoms has been used. The projections shown are the integral of the activity along the axes of the phantom

$$P_{side} = \int A\,dy \quad P_{front} = \int A\,dx \quad P_{top} = \int A\,dz.$$

From the ^{66}Ga measurement the activity in phantom B3 was reconstructed. To reduce the computational time only a $3 \times 3 \times 2$ cm part, centred on the activity containing tube, was reconstructed. The results from this reconstruction is shown in figure 4.14.
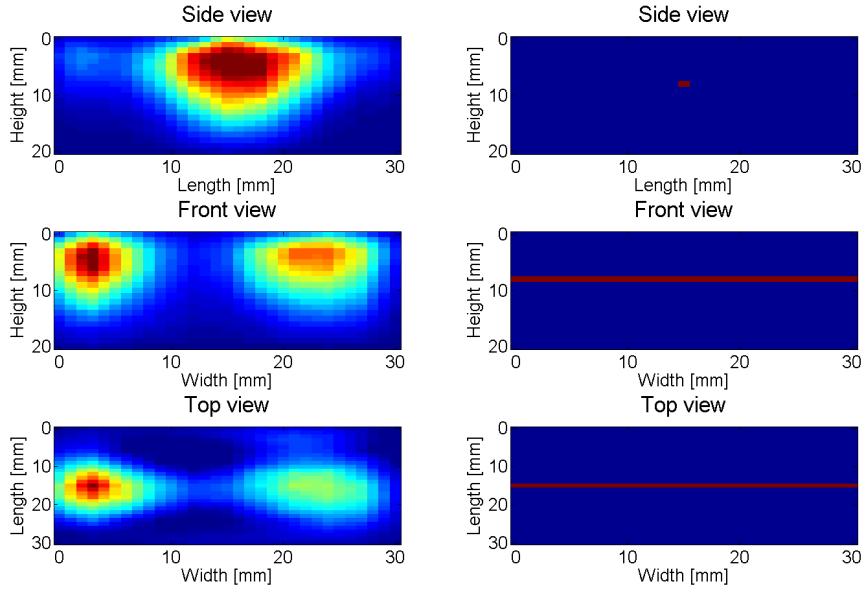

Figure 4.14: To the left, projections of the reconstructed activity in phantom B3 from the ^{66}Ga experiment. To the right, the projections of the tubes location.

The relative error of this optimization is characterized by $\varepsilon_{mean} = 10.9$ % and $\varepsilon_{max} = 31.1$ %. These errors are rather large, which could be due to a local minima being found or noise in the measurements.

The measurements from the ^{18}F were also reconstructed in a $3 \times 3 \times 2$ cm part of the phantom. The results from this reconstruction is displayed in figure 4.15.

The mean and maximum relative error for this optimization was $\varepsilon_{mean} = 0.3$ % and $\varepsilon_{max} = 1.5$ %. The reconstructed activity thus fits the measurements very well. These results indicate that not only the Cerenkov emission is being described by the reconstructed activity but also the measurement noise.

51
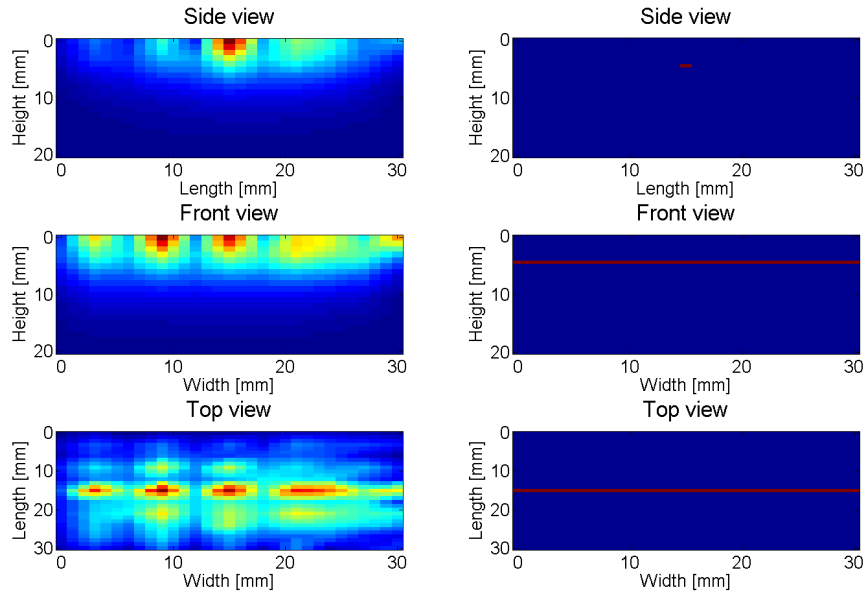
Figure 4.15: To the left, projections of the reconstructed activity from the ^{18}F experiment. To the right, the projections of the tubes location.

The PET/CT image of the phantom is shown in figure 4.16. PET is able to reconstruct the distribution of the ^{18}F within the tube with a high accuracy.
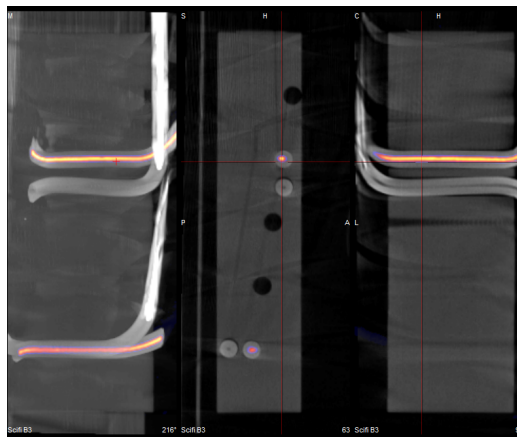

Figure 4.16: PET/CT image of phantom B3 containing ^{18}F. In these images it is the upper channel which has been used for the Cerenkov imaging.

5 DISCUSSION

5.1 Approximations

5.1.1 Continuous slowing down approximation

There were some differences in the predicted Cerenkov emission between CSDA and the Monte Carlo simulation. However the two methods did agree on the distance at which the Cerenkov emission ceased, roughly 4 mm for 1 MeV electrons. The total amount of Cerenkov radiation predicted were also similar, with the CSDA results deviation less than 5 % from the Monte Carlo simulation. The only significant difference were thus that CSDA predicted a lower emission close to the decay and a higher emission farther away. These results were based on decays in a single point and in practice with a spread out activity distribution this difference should be less prominent.

From these results it was concluded that CSDA yields a sufficiently accurate description of the electron deceleration for this work. However these results also indicate that replacing the CSDA with Monte Carlo simulations might improve the spatial distribution of the Cerenkov radiation. In that case the forward model would be more accurate and could potentially improve the spatial resolution of the inverse model.

5.1.2 Isotropic Cerenkov emission

The assumption of an isotropic Cerenkov source has not been individually verified. It is fairly common in medical optics to model directed sources as isotropic ones, with some modifications, due to the strong scattering in tissue. The alternative would be to model the directional dependence of the source, which in the case of CLI would require the paths of β-particles to be accurately described. Due to the stochastic nature of their interactions with a medium this would most likely require a Monte Carlo method to be employed. On top of that to capture the effects of the directional source the RTE would have to be solved for a directionally dependent radiance. This would increase the computational cost for solving the model to increase drastically.

5.1.3 NIRFAST SP_N

As expected the higher order methods gave better results than lower order, with the exception of SP_3 which deviated significantly close to the source. The reason for this unexpected behaviour was never found but is likely due to numerical instabilities. As earlier mentioned SP_5 and SP_7 produces very similar results and due to the higher computational cost SP_7 was neglected. Between the remaining SP_1 and SP_5 methods there were noticeable differences in performance, with SP_5 performing slightly better. The cost of SP_5 is that the stiffness matrix is of size $3N \times 3N$ compared to the $N \times N$ for SP_1. This causes the forward model to be solved slower since both matrix generation and equation solving is affected. This difference is further amplified in the inverse model where the forward model is solved multiple times.

Whether a higher order method is worthwhile or not will depend on the application. In the simulations and phantom experiments presented here the properties of the subjects are well controlled and higher order methods will likely yield better results. In more complicated cases, as *in vivo* studies, where there is uncertainties in optical properties the limiting factor might not be the order of the RTE approximation. In such cases higher order methods might thus be a wasted effort.

5.2 Results

5.2.1 Forward model

The spectra produced from the forward model were in good agreement with the expected results. The well-known λ^{-3} Cerenkov spectrum was accurately reproduced when the emission occurred in a transparent medium. For the tissue-like medium no reference spectrum was available but the optical properties in figure 2.1 seems to be well reflected. The tissue spectrum also has a similar shape as the one presented in [52].

The ^{66}Ga experimental results showed that the emission in phantoms B3 and C3 could be accurately reproduced with the forward model. In phantom D3 the simulated intensity deviated with about 25 % from the measurement. However the measurements from this phantom was weaker than the others and should thus be considered as the least reliable.

The width profile of the measured radiation was also fairly well reproduced by the forward model. Common for all three phantoms is that the measured value far from the peak intensity is slightly higher, this is likely due to noise or other effects not accounted for. From the measured image 4.9 it is clear that there is non-zero

measurements far away from the activity. The discrepancy is larger at the far end in figure 4.10, i.e at distance 25-30 mm. This is the end close to the boundary of the phantom which could introduce additional errors due to higher reflection than expected.

5.2.2 Inverse model

In the simulated test of the inverse model the measurements used to reconstruct were simulated intensities from the forward model. In this case it might seem like a perfect match would be achievable, since there obviously exist an activity distribution which will yield a zero fitting error. It is however not computationally feasible to use the intensities in all of the nodes in subject. This would not represent any realistic case either since actual measurements typically are external or possibly limited to a few internal locations. In this simulation 25 detector nodes were used, all located on the same side of the subject. From this limited amount of measurements 9261 unknowns are to be reconstructed, which as earlier mentioned will be an ill-posed problem. All things considered a perfect reconstruction is thus not expected.

The raw reconstructed activity was not that similar to the true activity. With the threshold operation 3.21 an activity distribution close to the true one was recovered. It should be noted that the threshold used were determined with perfect knowledge of the true activity distribution. It does however show that with perfect measurements and threshold it is possible to achieve an accurate reconstruction.

The reconstructions based on the experimental measurements did not agree with the known locations of the radioactive isotopes. The fitting errors for them were however small, indicating that they were in fact close to optimums of 2.34. This highlights the non-uniqueness of the problem, even if these activity distributions are decent candidates for the minimization, they are still not close to the desired solutions. There are several possible explanations to this behaviour. Mismatch between true and modelled optical properties might distort the results. The quality of the measurements are also very important, as the Cerenkov radiation is rather weak noise will have a large impact. This is probably the cause for the reconstructed activity in the ^{66}Ga reconstruction to be mainly located in two clusters. It has been shown that multi-spectral data should improve reconstructions [53]. The regularization of the problem also affects the reconstruction and it is possible that a different regularization strategy could yield better results.

5.3 Model Limitations

While the theory presented allows for a spatially dependant refractive index the implementation using a Cerenkov point source function only applies to the case where the refractive index does not change. This generalization would be straight-forward to implement, but will be more computationally costly as the source would have to be calculated for each node. This would especially affect the Jacobian calculation, where a source has to be calculated for each detector. In cases with constant refractive index the current implementation is thus preferable and these have been the only cases considered in this work.

In the current implementation detectors are only allowed to be located on the boundary of the subject. This was done to prevent detectors to be placed internally by mistake, as CLI classically is based on external measurements. It is however not unthinkable that internal measurements could be interesting in some settings. This modification would be very simple to make, as the forward model already calculates the fluence rate of light internally. The change would thus consist of allowing internal nodes to be marked as detectors and allow their nodal value to be extracted. Some additional boundary conditions between the subject and the detection device might also be required.

CONCLUSIONS

A forward model for the emission and propagation of Cerenkov radiation from β-particles has been formulated based on the theory of Frank and Tamm and radiative transport. This model maps an activity distribution of a known radionuclide within a subject, with known optical properties, onto the fluence rate within it. Notably the exiting radiation is calculated on the boundary, which allows for a direct comparison to external measurements.

The Cerenkov emission has been calculated using the continuous slowing down approximation for β-particles in tissue. The β-particles has been assumed to induce Cerenkov emission in all direction equally. The propagation of the emitted radiation has been described by the well-established radiative transport equation with partially reflective boundary conditions. In order to solve the radiative transport equation the simplified spherical harmonics approximations has been employed. Throughout this work the SP_5 method were employed.

From the forward model an inverse model has been developed. This model estimates the activity distribution within a subject given measurements of the radiation and optical properties. The inverse model is formulated as an optimization problem where the difference between the forward model and the measurements should be minimized. As the optimization problem typically is ill-posed regularization is required to stabilize it. To solve the optimization a Levenberg-Marquardt algorithm has been used, which inherently regularizes the problem.

A finite element method has been employed to solve the radiative transport equation in the forward model. The stiffness matrix required for this approach has been calculated using routines from NIRFAST. All implementation has been performed in Matlab, following the structure of NIRFAST's fluorescence routines.

Verification of assumptions and the models has mainly been performed through simulations and comparisons to Monte Carlo results. Two minor *in vitro* studies was also conducted for experimental validation. Results for the forward model were in general good and seemed to yield a fairly accurate description of the propagation of Cerenkov radiation. The inverse model produced acceptable results on simulated data but for the experimental data the results were not quite satisfactory.

OUTLOOK

Experimental studies have been very limited during this work and obviously a large-scale, systematic study would be very interesting. Things to investigate could include the resolution of the reconstructed activity, which would require the system to be calibrated to the forward model. Experimental reconstruction based on several spectral bands could also be of interest, as it may improve performance.

While the forward model produced good results it could of course be improved. As previously discussed it would be interesting to see the effects of a Monte Carlo based Cerenkov source term. The results of the inverse model was a bit disappointing and it will likely need to be improved before being used experimentally. Different regularization or optimization strategies could be of interest. As the inverse model is closely related to the forward model it is also highly likely that any improvements of the forward model will result in a better inverse model.

Although the forward model is working, it has limited practical use. If the inverse model could be modified to produce satisfactory reconstructions the performance of CLI as a method could be assessed. Such studies would thus not focus on the particular implementations presented in this work but rather the performance of CLI for different applications. Examples of such studies could include evaluation of xenograft tumour models and radiation therapy dose assessment, in particular from electron emitting compounds. The current model could also be extended to handle hybrid optical imaging modalities, such as Cerenkov excited fluorescence imaging.

AUTHOR REFLECTION

This has been the by far largest and most complex scientific project I have ever committed myself to. It has in many ways been challenging and I have had to use a wide range of my knowledge during this work. I have also gained a lot of new knowledge, mostly regarding the field of optical imaging and related methods. I do, however, believe that the most valuable lesson from this work will be the experience of working with the different parts of a large scale project, like this one. The general approach and method practiced in this project will almost certainly be of great use to me in future assignments.

The exposure to a scientific environment, where I have been able to partake in discussions has been enlightening and given me insight into the how research is conducted at a high level. For me, as a person with a genuine interest in science and technology, it has also been a great deal of fun.

To summarize I am very happy with the project, I have learned a lot and perhaps most importantly gained experience in working with a real-life problem. I am grateful to have been given this opportunity and I am confident that it has been a worthwhile experience.

ACKNOWLEDGEMENTS

I would like to thank the members of the biophotonics group at the division of atomic physics, department of physics, at LTH for providing a friendly and stimulating working environment. I am very grateful to have been given the opportunity to be a part of this group and work together with you.

I am also very grateful to Professor Stefan Anderson-Engels for showing me the beauties (and the horrors) of optical imaging in the first place. It was your teaching that sparked my interest for the subject and without it I may never have written this paper.

A special thanks to Erik Larsson for providing Monte Carlo simulations for the electron transport.

My deepest gratitude goes to Johan Axelsson for giving me this opportunity and guiding me through it, you have truly been an outstanding supervisor.

Finally, from the bottom of my heart, I would like to thank my family for their never-ending support and encouragement.

BIBLIOGRAPHY

[1] M. L. James and S. S. Gambhir. A molecular imaging primer: modalities, imaging agents, and applications. *Physiol. Rev.*, 92:897–965, 2012.

[2] N. Deshpande, A. Needles, and J. K. Willmann. Molecular ultrasound imaging: current status and future directions. *Clinical Radiology*, 65(7):567–581, 2010.

[3] R. Robertson, M. S. Germanos, C. Li, G. S. Mitchell, S. R. Cherry, and M. D. Silva. Optical imaging of Cerenkov light generation from positron-emitting radiotracers. *Physics in Medicine and Biology*, 54(16):N355, 2009.

[4] H. Ross. Measurement of β-emitting nuclides using Cerenkov radiation. *Analytical Chemistry*, 41(10):1260–1265, 1969.

[5] Y. Xu, E. Chang, H. Liu, H. Jiang, S. S. Gambhir, and Z. Cheng. Proof-of-Concept Study of Monitoring Cancer Drug Therapy with Cerenkov Luminescence Imaging. *Journal of Nuclear Medicine*, 53(2):312–317, 2012.

[6] Z. Hu, J. Liang, W. Yang, W. Fan, C. Li, X. Ma, X. Chen, X. Ma, X. Li, X. Qu, J. Wang, F. Cao, and J. Tian. Experimental Cerenkov luminescence tomography of the mouse model with SPECT imaging validation. *Opt Express*, 18(24):24441–24450, 2010.

[7] Z. Hu, X. Ma, X. Qu, W. Yang, J. Liang, J. Wang, and J. Tian. Three-dimensional Noninvasive Monitoring Iodine-131 Uptake in the Thyroid Using a Modified Cerenkov Luminescence Tomography Approach. *PLoS ONE*, 7(5):e37623, 2012.

[8] C. Li, G. S. Mitchell, and S. R. Cherry. Cerenkov luminescence tomography for small-animal imaging. *Optics Letters*, 35(7):1109 – 1111, 2010.

[9] H. Liu, G. Ren, Z. Miao, X. Zhang, X. Tang, P. Han, S. S. Gambhir, and Z. Cheng. Molecular Optical Imaging with Radioactive Probes. *PLoS ONE*, 5(3), 2010.

[10] R. Robertson, M. S. Germanos, M. G. Manfredi, P. G. Smith, and M. D. Silva. Multimodal imaging with (18)F-FDG PET and Cerenkov luminescence imaging after MLN4924 treatment in a human lymphoma xenograft model. *Journal of Nuclear Medicine*, 52(11):1764–1769, 2011.

[11] G. S. Mitchell, R. K. Gill, D. L. Boucher, C. Li, and S. R. Cherry. Cerenkov luminescence tomography for small-animal imaging. *Philosophical Transactions of the Royal Society A: Mathematical, Physical and Engineering Sciences*, 369(1955):4605–4619, 2011.

[12] A. E. Spinelli, C. Kuo, B. W. Rice, R. Calandrino, P. Marzola, A. Sbarbati, and F. Boschi. Multispectral Cerenkov luminescence tomography for small animal optical imaging. *Opt. Express*, 19(13):12605–12618, 2011.

[13] A. Ruggiero, J. P. Holland, J. S. Lewis, and J. Grimm. Cerenkov Luminescence Imaging of Medical Isotopes. *Journal of Nuclear Medicine*, 51(7):1123–1130, 2010.

[14] J. Zhong, C. Qin, X. Yang, S. Zhu, X. Zhang, and J. Tian. Cerenkov Luminescence Tomography for *In Vivo* Radiopharmaceutical Imaging. *International Journal of Biomedical Imaging*, 2011(Article ID 641618), 2011.

[15] S. Y. Jeong, M. H. Hwang, J. E. Kim, S. Kang, J. C. Park, J. Yoo, J. H. Ha, S. W. Lee, B. C. Ahn, and J. Lee. Combined Cerenkov luminescence and nuclear imaging of radioiodine in the thyroid gland and thyroid cancer cells expressing sodium iodide symporter: initial feasibility study. *Endocr J*, 58(7):575–583, 2011.

[16] A. E. Spinelli, M. Ferdeghini, C. Cavedon, E. Zivelonghi, R. Calandrino, A. Fenzi, A. Sbarbati, and F. Boschi. First human Cerenkography. *Journal of Biomedical Optics*, 18(2):020502–020502, 2013.

[17] H. Liu, C. M. Carpenter, H. Jiang, G. Pratx, C. Sun, M. P. Buchin, S. S. Gambhir, L. Xing, and Z. Cheng. Intraoperative Imaging of Tumors Using Cerenkov Luminescence Endoscopy: A Feasibility Experimental Study. *Journal of Nuclear Medicine*, 53(10):1579–1584, 2012.

[18] J. P. Holland, G. Normand, A. Ruggiero, J. S. Lewis, and J. Grimm. Intraoperative Imaging of Positron Emission Tomographic Radiotracers Using Cerenkov Luminescence Emissions. *Molecular Imaging*, 10(3):177 – 186, 2011.

[19] N. L. Ackerman and E. E. Graves. The potential for Cerenkov luminescence imaging of alpha-emitting radionuclides. *Physics in Medicine and Biology*, 57(3):771, 2012.

[20] D. L. J. Thorek, A. Ogirala, B. J. Beattie, and J. Grimm. Quantitative imaging of disease signatures through radioactive decay signal conversion. *Nature Medicine*, 19(10):1345–1350, 2013.

[21] R. S. Dothager, R. J. Goiffon, E. Jackson, S. Harpstrite, and D. Piwnica-Worms. Cerenkov Radiation Energy Transfer (CRET) Imaging: A Novel Method for Optical Imaging of PET Isotopes in Biological Systems. *PLoS ONE*, 5(10):e13300, 2010.

[22] M. A. Lewis, V. D. Kodibagkar, O. K. Öz, and R. P. Mason. On the potential for molecular imaging with Cerenkov luminescence. *Opt. Lett.*, 35(23):3889–3891, 2010.

[23] C. Ran, Z. Zhang, J. Hooker, and A. Moore. In Vivo Photoactivation Without "Light" Use of Cherenkov Radiation to Overcome the Penetration Limit of Light. *Mol Imaging Biol*, 14(2):156–162, 2011.

[24] J-L. Demers, S. C. Davis, R. Zhang, D. J. Gladstone, and B. W. Pogue. Čerenkov excited fluorescence tomography using external beam radiation. *Opt. Lett.*, 38(8):1364–1366, 2013.

[25] J. Axelsson, S. C. Davis, D. J. Gladstone, and B. W. Pogue. Cerenkov emission induced by external beam radiation stimulates molecular fluorescence. *Medical Physics*, 38(7):4127–4132, 2011.

[26] J. V. Jelley. *Čerenkov Radiation and its applications*. United Kingdom Atomic Energy Authority, 1958.

[27] L. Fülöp and T. Biró. Cherenkov radiation spectrum. *International Journal of Theoretical Physics*, 31(1):61–74, 1992.

[28] G. B. Collins and V. G. Reiling. Čerenkov Radiation. *Phys. Rev.*, 54:499–503, 1938.

[29] J. A. Rich, R. E. Slovacek, and F. J. Studer. Čerenkov Radiation from a Co^{60} Source in Water. *J. Opt. Soc. Am.*, 43(9):750–750, 1953.

[30] E. J. Konopinski. Beta-Decay. *Rev. Mod. Phys.*, 15:209–245, 1943.

[31] M. G. Stabin and C. Q. P. L. da Luz. New Decay Data For Internal and External Dose Assessment. *Health Phys.*, 83(4):471–475, 2002.

[32] S. M. Seltzer and M. J. Berger. Evaluation of the collision stopping power of elements and compounds for electrons and positrons. *The International Journal of Applied Radiation and Isotopes*, 33(11):1189 – 1218, 1982.

[33] S. M. Seltzer and M. J. Berger. Procedure for calculating the radiation stopping power for electrons. *The International Journal of Applied Radiation and Isotopes*, 33(11):1219 – 1226, 1982.

[34] M. J. Berger, J. S. Coursey, M. A. Zucker, and J. Chang. ESTAR, PSTAR, and ASTAR: Computer Programs for Calculating Stopping-Power and Range Tables for Electrons, Protons, and Helium Ions (version 1.2.3). [Online] Available: http://physics.nist.gov/Star [2013-08-29]. National Institute of Standards and Technology, Gaithersburg, MD.

[35] T. Tomimasu. Evidence for Positron-Electron Differences in Scintillation Response and Stopping Power. *Phys. Rev.*, 138:A268–A272, 1965.

[36] F. Rohrlich and B. C. Carlson. Positron-Electron Differences in Energy Loss and Multiple Scattering. *Phys. Rev.*, 93:38–44, 1954.

[37] R. Nachabe, B. H. Hendriks, M. van der Voort, A. E. Desjardins, and H. J. C. M. Sterenborg. Estimation of biological chromophores using diffuse optical spectroscopy: benefit of extending the UV-VIS wavelength range to include 1000 to 1600 nm. *Biomed. Opt. Express*, 1(5):1432–1442, 2010.

[38] S. L. Jacques. Optical properties of biological tissues: a review. *Physics in Medicine and Biology*, 58(11):R37, 2013.

[39] L. C. Henyey and J. L.Greenstein. Diffuse radiation in the Galaxy. *The Astrophysical Journal*, 1941.

[40] A. D. Klose and E. W. Larsen. Light transport in biological tissue based on the simplified spherical harmonics equations. *Journal of Computational Physics*, 220(1):441 – 470, 2006.

[41] E. W. Larsen, J. E. Morel, and J. M. McGhee. *Asymptotic derivation of the multigroup P_1 and Simplified P_N equations with anisotropic scattering.* 1994.

[42] G. C. Pomraning. Asymptotic and variational derivations of the simplified P_N equations. *Annals of Nuclear Energy*, 20(9):623 – 637, 1993.

[43] R. T. Ackroyd, C. R. E. de Oliveira, A. Zolfaghari, and A. J. H. Goddard. On a rigorous resolution of the transport equation into a system of diffusion-like equations. *Progress in Nuclear Energy*, 35(1):1 – 64, 1999.

[44] J. Zhong, J. Tian, X. Yang, and C. Qin. Whole-Body Cerenkov Luminescence Tomography with the Finite Element SP_3 Method. *Annals of Biomedical Engineering*, 39(6):1728–1735, 2011.

[45] M. Jermyn, H. Ghadyani, M. A. Mastanduno, W. Turner, S. C. Davis, H. Dehghani, and B. W. Pogue. Fast segmentation and high-quality three-dimensional volume mesh creation from medical images for diffuse optical tomography. *Journal of Biomedical Optics*, 18(8):086007–086007, 2013.

[46] H. Dehghani, P. K. Yalavarthy M. E. Eames, S. C. Davis, S. Srinivasan, C. M. Carpenter, B. W. Pogue, and K. D. Paulsen. Near infrared optical tomography using NIRFAST: Algorithm for numerical model and image reconstruction. *Communications in Numerical Methods in Engineering*, 25:711–732, 2009.

[47] S. R. Arridge. Optical tomography in medical imaging. *Inverse Problems*, 15(2):R41, 1999.

[48] S. R. Arridge and J. C. Schotland. Optical tomography: forward and inverse problems. *Inverse Problems*, 25(12):123010, 2009.

[49] E. Mellhammar. Performance Assessment of Cerenkov Emission Imaging. Master's thesis, Department of Physics and Department of Medical Radiation Physics, Lund University, 2013. `http://www.lunduniversity.lu.se/o.o.i.s?id=24965&postid=4192067`.

[50] J. Swartling, J. S. Dam, and S. Andersson-Engels. Comparison of Spatially and Temporally Resolved Diffuse-Reflectance Measurement Systems for Determination of Biomedical Optical Properties. *Appl. Opt.*, 42(22):4612–4620, 2003.

[51] Andor. `http://www.andor.com/scientific-cameras/ikon-ccd-camera-series/ikon-m-934`. Accessed: 2014-02-03.

[52] A. E. Spinelli and F. Boschi. Optimizing in vivo small animal Cerenkov luminescence imaging. *Journal of Biomedical Optics*, 17(4):4–6, 2012.

[53] H. Dehghani, S. C. Davis, and B. W. Pogue. Spectrally resolved bioluminescence tomography using the reciprocity approach. *Med. Phys.*, 35(11):4863–71, 2008.